Enhancing electrocatalytic water splitting by strain engineering

You, Bo; Tang, Michael T.; Tsai, Charlie; Abild-Pedersen, Frank; Zheng, Xiaolin; Li, Hong

2019

You, B., Tang, M. T., Tsai, C., Abild-Pedersen, F., Zheng, X., & Li, H. (2019). Enhancing electrocatalytic water splitting by strain engineering. Advanced Materials, 31(17), 1807001-. doi:10.1002/adma.201807001

https://hdl.handle.net/10356/142181

https://doi.org/10.1002/adma.201807001

WILEY-VCH

DOI: 10.1002/ ((please add manuscript number))
Article type: Review

Enhancing Electrocatalytic Water Splitting by Strain Engineering

Bo You†, Michael T Tang†, Charlie Tsai, Frank Abild-Pedersen, Xiaolin Zheng, and Hong Li († equal contribution)*

Dr. B. You, Prof. H. Li
School of Mechanical and Aerospace Engineering
Nanyang Technological University, 639798, Singapore
E-mail: ehongli@ntu.edu.sg
M. T. Tang, Dr. C. Tsai
SUNCAT Center for Interface Science and Catalysis
Department of Chemical Engineering
Stanford University
California 94305, USA
Dr. F. Abild-Pedersen
SUNCAT Center for Interface Science and Catalysis
SLAC National Accelerator Laboratory
California 94025, USA
Prof. X. Zheng
Department of Mechanical Engineering
Stanford University
California 94305, USA
Prof. H. Li
School of Electrical and Electronic Engineering
CINTRA CNRS/NTU/THALES, UMI 3288, Research Techno Plaza
Nanyang Technological University, 639798, Singapore

Keywords: water splitting, electrocatalyst, strain engineering, two-dimensional materials, DFT modeling

Electrochemical water splitting driven by sustainable energy such as solar, wind and tide, is attracting ever-increasing attention for sustainable production of clean hydrogen from water. Leveraging these advances requires efficient and earth-abundant catalysts to accelerate the kinetically sluggish hydrogen and oxygen evolution reactions (HER and OER). A large number of advanced water splitting electrocatalysts have been developed through recent understanding of the electrochemical nature and diverse nanostructuring techniques. Specifically, strain engineering offers a novel route to promote the electrocatalytic HER/OER performance for efficient water splitting. Herein, the recent theoretical and experimental progresses of applying strain to enhance heterogeneous electrocatalysts for both HER and

OER are reviewed, and then the future opportunities are discussed. The review begins with a brief introduction of the fundamentals of water splitting reactions, and the rationalization for utilizing mechanical strain to tune an electrocatalyst. Afterward, the recent advances on strain-promoted HER and OER are discussed, with special emphasis given to combined theoretical and experimental approaches for determining the optimum straining effect for catalysis, and experimental approaches for creating and characterizing strain in nanocatalysts particularly the emerging two-dimensional nanomaterials. Finally, a vision for a future sustainable hydrogen fuel community based on strain-promoted water electrolysis is proposed.

1. Introduction

There has been a rapid continuous increase in global demands for energy within the last few decades.[1-3] It is expected that global power consumption (~18 TW nowadays) may triple by 2100.[4] Due to their high energy density, fossil fuels such as coal, petroleum and natural gas, have been exploited as the main energy source for our economy and society since the era of industrialization despite their detrimental effects on the climate and health of the planet.[5] For example, the carbon dioxide emitted by fossil fuel sources is believed to be responsible for climate change, air pollution, desertification and ocean acidification.[1] Because of the growing concerns regarding the consequence of society's continued dependence on fossil fuels, the interest in development of sustainable alternative energy solutions has increased dramatically.[1-5]

The energy at the Earth's surface irradiated by the Sun for 80 min is sufficient to satisfy the annual global demand based on current consumption rate.[4, 6, 7] However, solar irradiation is often intermittent, and separated in time and location from consumption, thus requiring efficient energy storage and transport systems.[4,6,7] Electrochemical or photoelectrochemical

water splitting to produce hydrogen is an attractive strategy for solar energy storage because hydrogen gas as a product can be stored, distributed, and used on demand, and the reverse process generates water as the only product.[3, 4, 6-8] The water splitting reaction ($H_2O \rightarrow H_2+1/2O_2$) consists of two half-reactions, namely the hydrogen evolution reaction (HER) and oxygen evolution reaction (OER), which occur on the cathode and anode, respectively.[3] Depending on the reaction conditions, the two half-reactions can be expressed in different ways:

(a) in acidic solution

cathode: $2H^+ + 2e^- \rightarrow H_2$ (Equation 1)

anode: $H_2O \rightarrow 2H^+ + 1/2O_2 + 2e^-$ (Equation 2)

(b) in neutral solution

cathode: $2H_2O + 2e^- \rightarrow H_2 + 2OH^-$ (Equation 3)

anode: $H_2O \rightarrow 2H^+ + 1/2O_2 + 2e^-$ (Equation 4)

(c) in alkaline solution

cathode: $2H_2O + 2e^- \rightarrow H_2 + 2OH^-$ (Equation 5)

anode: $2OH^- \rightarrow H_2O + 1/2O_2 + 2e^-$ (Equation 6)

Under standard conditions, a thermodynamic potential of 1.23 V is required to achieve electrochemical water splitting, which corresponds to an energy input of ΔG = 237.1 kJ mol^{-1}. Unfortunately, the sluggish kinetics of both HER and OER require additional overpotentials (the potential difference between the thermodynamic potential and the experimental potential) to reach an appreciable catalytic current density, resulting in relatively low energy conversion efficiencies.[9-14] Thus, the practical potential for water splitting is much larger than 1.23 V, which can be described as:

$$E_{op}=1.23\ V + \eta_a + \eta_c + \eta_{other} \quad \text{(Equation 7)}$$

wherein, η_a and η_c represent the anode and cathode overpotentials, respectively, and η_{other} is the total voltage drop on other parasitic resistances in the electrochemical cell, including

solution resistance, contact resistance, membrane resistance, *etc*. The η_a and η_c result from the unfavorably high energies required for the formation of reaction intermediates on the electrode surface.[15] The resulting overpotential needed to drive the reaction is one of the most important parameters that significantly influence the output performance of water splitting devices. The most critical problem is how to effectively catalyze the reactions on both electrodes to promote their reactive kinetics to achieve low overpotentials and thus high energy conversion efficiencies. In general, the kinetic of the two-electron transfer process in HER is faster than that of the multistep proton-coupled electron transfer process in OER (four-electron).[16-18]

Currently, the state-of-the-art catalysts to split water in acidic media are iridium and ruthenium-based materials for the OER and Pt composites for the HER,[19] requiring a cell voltage of ~1.50 V to achieve a current density of 10 mA cm^{-2}.[20] Unfortunately, the high material cost and scarcity prohibit a large-scale implementation. Consequently, great efforts have been devoted to designing and synthesizing cost-effective alternatives. For the HER, transition-metal alloys, nitrides, sulfides, carbides, phosphides and selenides, have shown promising catalytic performance;[21] and, for the OER, many noble-metal-free catalysts based on transition-metal oxides, hydroxides, oxy-hydroxides and perovskite oxides have been developed with superior catalytic performances.[4, 5] To further promote these candidates' catalytic performance for water splitting, diverse techniques have been exploited for the underlying catalysts, such as tailoring the interface structure,[9, 22-25] controlling particle size, shape, dimensionality, composition and introducing defects,[26] along with external excitation including light, magnetism, and electric field.[27-29]

Among them, strain engineering for nanostructures has gained momentum in recent years; and it has proven to be a powerful method in tailoring the surface electronic structure and the catalytic properties of nanomaterials, thus rendering it fundamentally and technologically important for a wide range of applications.[30-32] Strain (unit: dimensionless) is the

deformation of a solid caused by stress (unit: Pa) that is defined as the external force acting on a unit area. Deformations that can recover upon the stress removal are elastic deformation (or elastic strain) that is reversible. In contrast, plastic deformation (plastic strain) is irreversible.[30] Since plastic deformation is typically associated with a dislocation of the lattice, it could seriously disturb the original electronic structure of the material; and thus is much less pronounced in engineering applications. Thus, in this review, we limit ourselves to elastic strain unless stated otherwise. Depending on the relative direction of external force to the stressed area, one may have tensile strain that stretches or lengthens the solid, compressive strain that compresses or shortens the solid, or shear strain that shears the solid. All these elastic strains could alter the electronic structure and chemical reactivity of materials to a certain extent, and thus finds many engineering applications. For instance, strain engineering has achieved a tremendous success in CMOS technology, where the electron mobility in silicon is greatly enhanced by tensile strain induced by lattice mismatch or capping layer.[33, 34] Such strained silicon are used by almost all microprocessor manufacturers. Elastic strain also finds applications in chemical engineering involving polymer, oxide and membrane.[35, 36] The energy landscapes of chemical reactions can be modulated by elastic strain, which is sometimes termed as mechano-chemical coupling.[37] The strain-induced reactivity particularly on metal surface has also been studied extensively for a few decades.[38, 39] In recent years, the potential of strain engineering in catalysis and energy applications is attracting ever-increasing attention.[40-46] In this review, we focus on the impact of elastic strain engineering in electrochemical water splitting reactions (HER and OER).

In conjunction with the experimental design and synthesis of water splitting catalysts, a large amount of efforts have been devoted to understanding them with computational chemistry, especially using density functional theory (DFT).[47-50] Experiments that directly measure the binding energies of intermediates are often challenging to perform; therefore in complex catalyst designs involving multiple attributes including strain, computational

techniques are crucial in forming a quantitative correlation between the energetics of intermediates and observed electrocatalytic kinetics.[2] Specifically, DFT provides an atomistic understanding of water splitting electrocatalysis and the guidance needed in the design of improved HER and OER electrocatalysts. [2, 11] [49] For example, the Gibbs free energy change (ΔG_H*) of the adsorbed hydrogen on active site of a catalyst (denoted as M-H*) has been calculated for a large number of HER catalysts and employed successfully as a descriptor in predicting HER trends for a large number of catalyst candidates in acidic media.[48, 49] According to the Sabatier principle, an ideal catalyst should have a ΔG_H* close to zero, which means that it not only possesses sufficient affinity to bind hydrogen atoms to facilitate the initial proton-coupled electron transfer process, but also have enough repellency to facilitate the M-H* bond breaking and thus formation of gaseous H_2.[13] Similarly, activity trends and descriptors for a variety of OER electrocatalysts have been developed.[50] At present, DFT has been extended to many other emerging clean energy-related reactions such as hydrogen peroxide production,[51] oxygen and carbon dioxide reduction,[50, 52] and nitrogen fixation.[50, 53-55]

Herein, we summarize recent progress in strain engineering of diverse electrocatalysts from precious metals to transition-metal-based compounds for enhanced water splitting reaction (HER and OER). We strive to identify the individual contribution of strain though it is usually mixed with other engineering effects. In particular, we intend to show how DFT can be effectively applied to guide the design of highly active electrocatalysts such as strained two-dimensional nanomaterials. Afterwards, we will present detailed discussion on how strained systems are synthesized and characterized experimentally, as well as their impacts on electrocatalytic HER and OER performances. Finally, a perspective on the challenges and opportunities of this field is provided.

2. Optimization of Catalyst Through Rational Design Principles

Theoretical work in the past decade based on DFT has allowed us to identify details of the mechanism for many chemical reactions. The calculated energies can be used to illustrate the variations in free energy of electrochemical catalytic reactions,[56] which allow us to see the energy landscapes of chemical reactions, and then identify which intermediate steps are rate-limiting for an overall reaction process. From the energy landscape, we can explain the overpotential phenomena seen with existing catalytic systems, determine the limiting intermediate step for the entire reaction process, as well as rationalize why strain can be used to tune energetics. A microkinetic model can then be used to determine where all known catalytic systems lie on a rate-volcano, which we will briefly discuss next before diving into the use of strain to optimize catalytic systems.[57-60]

2.1. Scaling Relations and Volcanos for Hydrogen and Oxygen Evolution Reactions

After determining the reaction mechanisms using DFT, we can use scaling relations – linear correlations between intermediate binding energies – to create a simplified model that describes the overall reaction rate. The rate is visualized by a volcano plot, which is a simple mapping that depends on a limited number of intermediate binding energies. A rate-volcano will have an optimum that corresponds to the point with the highest rate on the volcano plot. This allows us to rationalize the design of new catalysts by modifying the active sites so that intermediate binding energies are close to the optimal point on volcano.

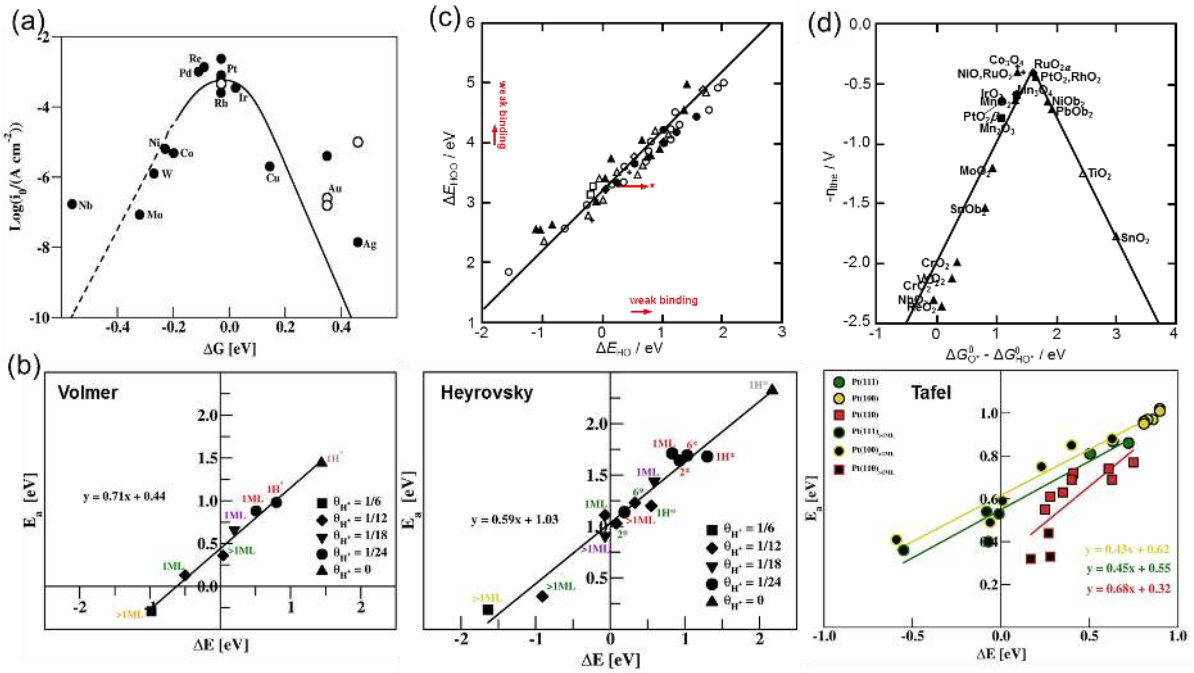

Figure 1. Scaling relations and Volcano curves for HER and OER. (a) Hydrogen free binding energy vs. activity; circles represent experimental data, the curve is from microkinetic theory. (b) Scaling relation between hydrogen free binding energy and activation barrier for each elementary HER step. Reproduced with permission.[61] Copyright 2010 American Chemical Society. (c) Scaling between adsorption of OH* and OOH* for OER on perovskites (circles), rutile oxides (triangles), Mn_xO_y (squares), anatase oxides (diamonds), Co_3O_4 (plusses). Solid circles are adsorption energies on high coverage surfaces. (d) Overpotential volcano for OER with regards to free binding energy differences between O* and OH*. Ruthenium oxides are found to have the ideal surfaces. Reproduced with permission.[62] Copyright 2011, Wiley-VCH.

Various catalytic systems lie on different part of the HER or OER volcano. Using a series of H binding energy calculations on different catalytic surfaces, Nørskov and co-workers' group laid out a HER rate volcano, as shown in **Figure 1**a.[61] The volcano for HER shows the exchange current density for HER versus the free binding energy of hydrogen on different transition-metal surfaces at 0 V. The volcano makes it clear that the optimal binding energy of H for HER is at 0 eV. The open circles represent experimental (111) single crystal surfaces, whereas the filled circles represent experimental polycrystalline surfaces data. The peak of the volcano is populated with Pt, Re, Pd, Ir, and Rh surfaces that are among the best HER catalysts verified experimentally. The correlation between experimental results and the theoretical predictions demonstrates how DFT capture the underlying trends among transition-metal surfaces regarding

HER electrocatalysis (Figure 1a). Figure 1b also captures an important insight for the HER reaction with regards to all three elementary steps: Volmer, Heyrovsky, and Tafel steps, *i.e.*, the H binding energy scales with the activation energy for forming H_2 gas. The weaker the H binding energy is, the larger the barrier to form H_2 becomes. Likewise, a stronger H binding energy is associated with a lower barrier to form H_2, which could potentially lead to poisoning of the surface with adsorbed hydrogen.

Similarly, a generalized scaling relation between OH* and OOH* has been found in OER, as shown in Figure 1c.[62] As a result, a volcano, as shown in Figure 1d, can be formed, showing that the overpotential for OER is determined by the binding energy difference between OH* and OOH*, where a difference of 1.23 eV would lead to an overpotential of zero for the reaction. Thus, in order to optimize OER performance, ways to stabilize OOH* with respect to OH* needs to be identified.[63] We will now apply this theoretical framework to the effects of strain on surfaces at the atomic level.

2.2. Origin of Strain Effect on Adsorption Energy

Scaling relations and volcano plots suggest that materials with certain binding energies in a well-defined range should possess the optimal reaction rates. This awareness enables the tuning of poorly performing systems towards superior ones through electronic and mechanical engineering of the catalyst. DFT has also been used to examine the origins of surface strain effects on binding energies by aggregating data across various metal systems with and without applied strain. The schematic, as shown in **Figure 2**a, indicates shifting of the *d*-band center of late transition metals (with *d*-band more than half filled) with tensile strain.[30] In the absence of strain, the *d*-band center usually shifts with respect to the metal atom's local coordination environment. That is, the change in *d*-band center comes from changes in the number of neighboring metal atoms; lowering the coordination leads to smaller local bandwidth and a higher *d*-band center. Evidently, tensile strain lowers the coordination

numbers and thus gives rise to the reduced bandwidth and an upshift of *d*-band center (Figure 2a). Compressive lattice strain has the opposite effect, causing a broadening of the bands and resulting in a downward shift of the *d*-band center.

The *d*-band center is important because the interaction between the adsorbate states and the metal *d* states is crucial for the interaction energy. While the *sp* bands of the metal are broad and structureless, the *d* bands are narrow; and thus small changes in the environment can change the *d* states and their interaction with adsorbate states significantly. As the *d*-band center shifts, the unoccupied anti-bonding states will also shift up or down accordingly.[39] Compressive lattice strain causes an increased overlapping of the *d*-orbitals of metal atoms. This overlap will increase the bandwidth and lower the *d*-band center energy, thereby pushing more anti-bonding states below the Fermi level and allowing adsorbates to interact with them. This weakens the binding energies of adsorbates. Tensile lattice strain has the opposite effect.[30] For example, upshifting the *d*-band center ($\delta\varepsilon_d$) of Pd overlayers results in higher hydrogen adsorption energy (E_{SCE}, Figure 2b). Similarly, change in the *d*-band center energy of Pt and Au will also alter the O adsorption energies (Figure 2c). Similar to the *d*-band theory of metals, an electronic theory can be applied to transition-metals compounds such as molybedenum disulfide (MoS_2) for H, O and OH adsorption (Figure 2d and 2e).[47]. All H, O and OH intermediates adsorptions are widely investigated in water splitting reactions using this thoeretical framework.

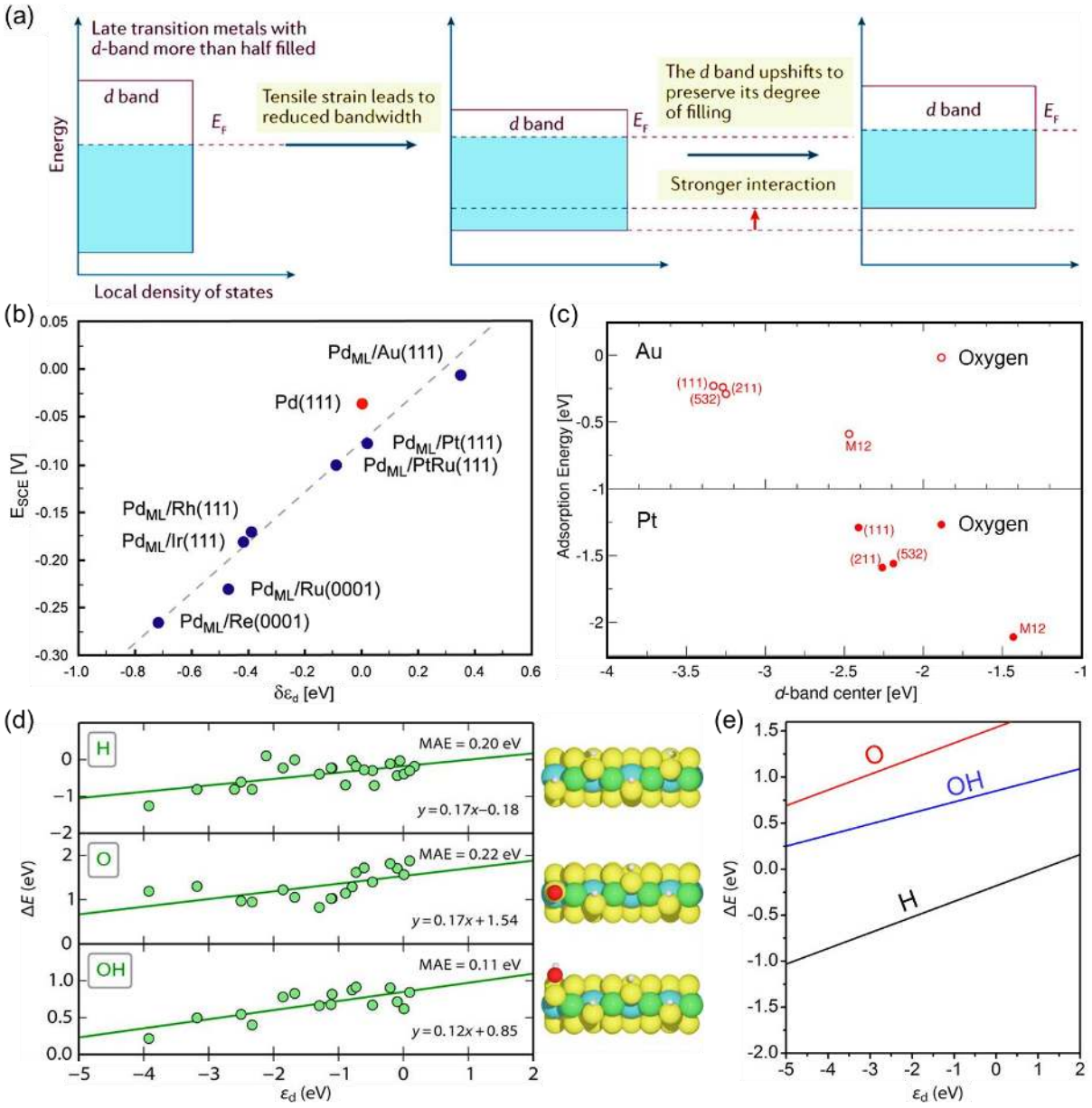

Figure 2. Mechanisms for strain-enhanced HER and OER. (a) Energy diagrams explaining the effect of tensile strain on the *d* band position of late transition metals. Reproduced with permission.[30] Copyright 2017 Springer Nature. (b) Electrochemically measured changes in the hydrogen adsorption energy (E_{SCE}) for Pd overlayers on a number of metals versus the calculated shift of the *d*-band center ($\delta\varepsilon_d$). (c) O adsorption energies for a range of different Pt and Au surfaces including 12 atom clusters versus the calculated *d*-band center (ε_d). Reproduced with permission.[39] Copyright 2011 National Academy of Sciences of the United States of America. (d,e) Adsorption energy of various key reaction intermediates ΔE as a function of the *d*-band center ε_d. H, O and OH are adsorbed onto S sites at the stable S and H coverages (blue = Mo, yellow = S, white = H, red = O). Reproduced with permission.[47] Copyright 2014 American Physical Society.

2.3. Combining Theory and Experiments for Strained Water-Splitting Catalysis

As discussed earlier, elastic lattice strain can be used to rationally design new catalytic systems because it provides a way to modify binding energies of intermediates by altering the electronic state at the Fermi level. We now discuss about some examples of catalytic systems where theoretical understanding of reaction mechanisms and the effects of strain meet experimental results in tuning intermediate binding energies for optimizing catalytic performance.

A particular strategy for inducing surface lattice strain and tuning adsorption energies of intermediates is through thinly coated metal alloy surfaces or core-shell structures. The surface structure will induce a lattice mismatch effect, which strains the immediate surface. High-throughput alloy screening has been employed to find ideal blends of metal on metal that improve the overall performances of HER and OER on a given surfaces. **Figure 3**a shows a table of free binding energy of hydrogen on solute layer on host substrate metal surface.[48] The table is then used to perform high-throughput screening to find an optimal surface compliment for HER. Experimental studies have successfully observed this effect when bimetallic PtBi alloys are created as shown in Figure 3b and 3c.

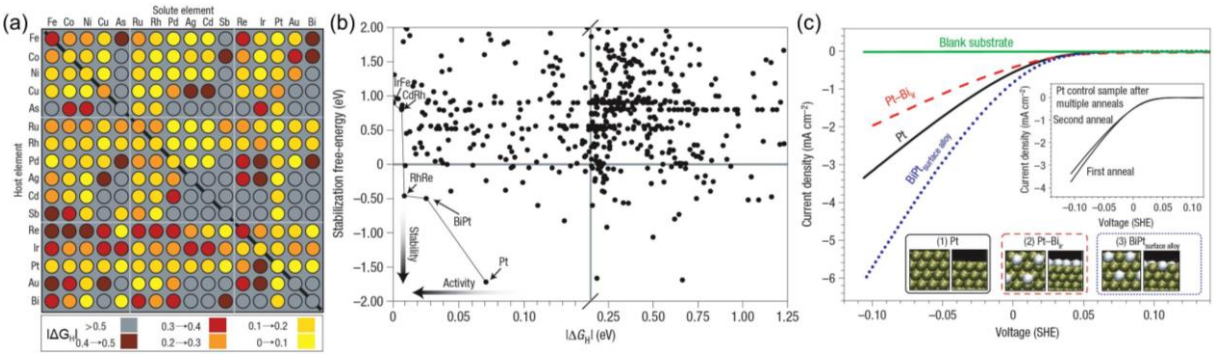

Figure 3. Strained metal catalysts for HER. (a) Heat map table of hydrogen free binding energy, with solute metal over substrate host metal. (b) High throughput analysis plot of surface stability and HER activity. PtBi alloy is found to be optimal for HER at the lower left corner. (c) Experimental HER current density of Bi on Pt substrate vs. Pt vs. Pt-Bi alloy mixture, demonstrating the effects of surface lattice strain on HER performance. Reproduced with permission.[48] Copyright 2006 Springer Nature.

Another notable system that can utilize lattice strain is one of the transition-metal chalcogenides (TMDs), MoS_2, a bio-inspired catalyst for HER. This two-dimensional (2D) material was found to possess edge sites that are similar to the nitrogenase enzyme's metal center coordination environment, which were found to have H binding energies close to the optimal value for HER.[64] The edge sites were initially rationalized to be active based on the volcano curves and free energy diagrams of HER, however, the basal plane can also be rationalized to be very active when S-vacancies are introduced and strain is applied (**Figure 4**a-e).[65] Theoretical and experimental results show that the S-vacancies are new catalytic sites in the basal plane; and the resulted gap states around the Fermi level allow hydrogen to bind directly to expose Mo atoms (Figure 4d). Then the free energy (ΔG_H) of the adsorbed H on the basal surface can be altered by straining the surface with S-vacancies; allowing us to fine-tune the binding energies of the basal plane sites to improve activity (Figure 4b and 4c). A clear volcano relation emerges when the intrinsic HER activity ($TOF_{S\text{-}vacancy}$) is plotted versus ΔG_H (Figure 4e), suggesting that (1) the experimental and theoretical investigations nicely complement each other, and (2) ΔG_H is indeed a good descriptor for predicting HER activity in these new active sites. However, it is worth noting that strain decreases the stability of the MoS_2 with vacancies; which could be described by the increase of surface energy (Figure 4f). Likewise, additional experiments partook in devising new ways to introduce S-vacancies to the basal plane of MoS_2; plasma is the usual way to do so, whereas it is also possible to desulfurize the basal plane electrochemically when at least -1.0 V is applied, albeit producing hydrogen disulfide in the process.[66]

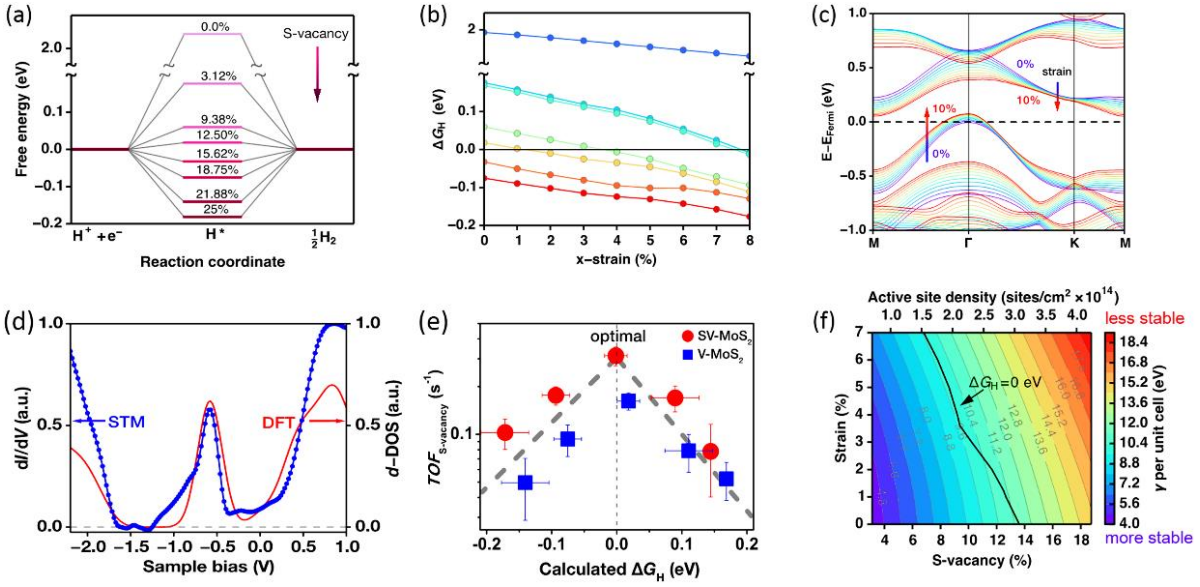

Figure 4. Strain effect in MoS_2 with S-vacancies for HER. (a) Calculated free energy versus the HER reaction coordinates as a function of S-vacancy percentage. (b) ΔG_H versus %x-strain (uniaxial tensile strain along x-axis) at various S-vacancy percentages. (c) Calculated E-κ relation of a monolayer MoS_2 under tensile strain from 1 to 10%. The tensile strain tends to decrease the band gap. (d) Measured differential conductance dI/dV (left y-axis) and DFT calculated *d*-orbital density of states on the Mo atom of the S-vacancy (right y-axis) as a function of sample bias for monolayer MoS_2 with 12.5% S-vacancy. (e) Experimental $TOF_{S\text{-vacancy}}$ (normalized to number of S-vacancy) versus their corresponding calculated ΔG_H for MoS_2 with S-vacancies before strain (V-MoS_2; solid blue squares) and after strain (SV-MoS_2; solid red circles). A volcano relation indicated by dashed line appears. (f) Colored contour plot of surface energy per unit cell γ (with respect to the bulk MoS_2) as a function of S-vacancy and uniaxial strain. Reproduced with permission.[65] Copyright 2016 Springer Nature.

3. Experimental Creation of Strain

Depending on the properties of the catalyst, one straining method could work better than the other on a particular catalyst. We organize this section according the structure of the nanoscale catalyst. We discuss the non-two-dimensional (quantum dot, nanocube, nanoparticle, nanowires, nanotubes *etc*.) nanocatalyst first, followed by the emerging two-dimensional (graphene-like nanosheets) catalysts.

3.1. Non-Two-Dimensional Nanocatalysts

3.1.1. Morphology Modulation Induced Strain

Morphology is intimately related to lattice strain due to the anisotropic nature of nanopolyhedral geometries (**Figure 5**). Shape-controlled synthesis of nanocrystals can create special configurations that strongly deviate from the classical Wulff construction, producing high surface energy facets, vertices and edges. Owing to the under-coordinated properties, those surface atoms at vertices and edges have to be stabilized by inward displacement from their regular lattice positions, giving rise to an effectively higher coordination number. At the meantime, the surrounding atoms prefer to displace inward to adapt the contracted edge and corner atoms. This effect generates a strain gradient, distinctly different areas for surface interactions and thus distinctive catalytic behaviors.[31] Similarly, creating porosity can also create the dangling surface atoms and strain gradient.[26]

Crystal Shaping Induced Strain

The crystal shape-strain correlation has been reported by Scardi's group through the simulated X-ray diffraction patterns of a cube, a cuboctahedron, and an octahedron nanocrystal morphologies (Figure 5a-d).[67] It is demonstrated that the subtle satellite peaks at the base of the main diffraction peaks are different between the shaped nanocrystals. This is characteristic for anisotropic strain gradients (corner/edge compression versus facet expansion) in each shape.

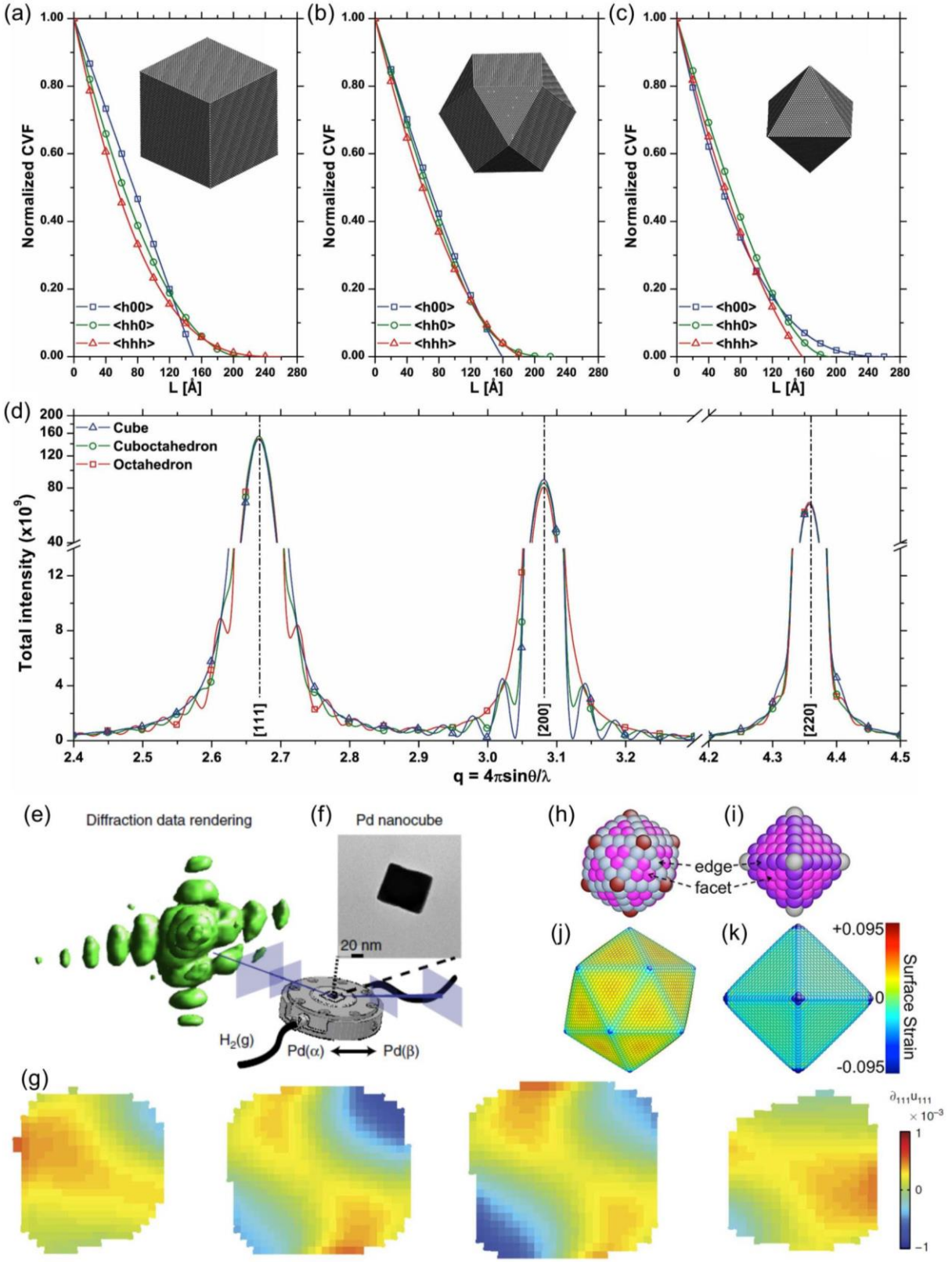

Figure 5. Crystal shaping induced strain. Examples of common volume function (CVFs) for a (a) cube, (b) cuboctahedron, and (c) octahedron. (d) The corresponding simulated powder patterns show the unique fingerprints from satellites around the main peaks for different morphologies. Reprinted with permission.[67] Copyright 2012 Wiley-VCH. (e) Isosurface rendering of the diffraction data obtained from an α phase Pd nanocube. (f) SEM image of a Pd nanocube on a silicon substrate. (g) The measured compressive/tensile strain distribution.

Reproduced with permission.[68] Copyright 2015 Springer Nature. Atomic structures of (h) Pt icosahedral cluster with 309 atoms and (i) Pt octahedral cluster with 146 atoms. Different color means different coordination number. Surface strain fields of Pt (j) icosahedral and (k) octahedral nanocrystals with diameter of 10 nm. Color indicates strain labeled in the color map. Reproduced with permission.[69] Copyright 2012 American Chemical Society.

Recently, three-dimensional (3D) strain field on a single nanocrystal was also resolved via coherent X-ray diffractive imaging (CXDI). CXDI is an in-situ X-ray imaging technique capable of resolving 3D strain distributions in reactive environments. In Bragg geometry, X-ray sensitive area detectors are used to record scattered coherent X-rays. Phase-retrieval algorithms are then employed to reconstruct the 3D electron density and lattice displacement fields in single nanocrystals.[68] The penetrating power of high energy X-rays and 3D resolving capability make CXDI an ideal tool for in-situ studying and understanding the complex role of crystallographic facets, defects, and surface effects in nanoscale dynamics. Ulvestad *et al.* used the CXDI to reveal strain information in individual Pd nanocubes by comparing experimental results with a 3D phase field model. The scheme of experimental set-up is shown in Figure 5e. Pd nanocubes on a silicon substrate (Figure 5f) are included in a gas environmental X-ray cell, wherein the focused coherent X-rays are incident on it. Figure 5f shows an isosurface rendering of a (111) diffraction pattern from an individual Pd nanocube. The diffraction intensity is proportional to the Fourier transform of the electron density and thus is similar to the Fourier transform of a cube. By computing from an average of the reconstructions, the measured strain distribution in a β phase nanocube can be obtained (Figure 5g), which agrees well with the strain distribution computed by the phase-field model. As known, coordination numbers (CN) of atoms on the edge of icosahedral and octahedral nanoparticles are 8 and 7, respectively; but 9 on (111) facets (Figure 5h and 5i).[69] These differences would induce various strains and thus diverse catalytic activity. By means of molecular dynamics (MD) simulations, Yang's group obtained the strain fields on the surface of icosahedral and octahedral Pt nanocrystals with a diameter of 10 nm.[69] As shown in

Figure 5j and 5k, the surface strain on an icosahedral nanoparticle is tensile (averaging +1.6%), while it is compressive (averaging -1.6%) on an octahedral nanoparticle.

Porosity Controlling Induced Strain

The high porosity for nanocatalysts is generally considered to be beneficial for improvement of electrocatalytic activities and decrease of mass loading due to the high accessibility of active sites.

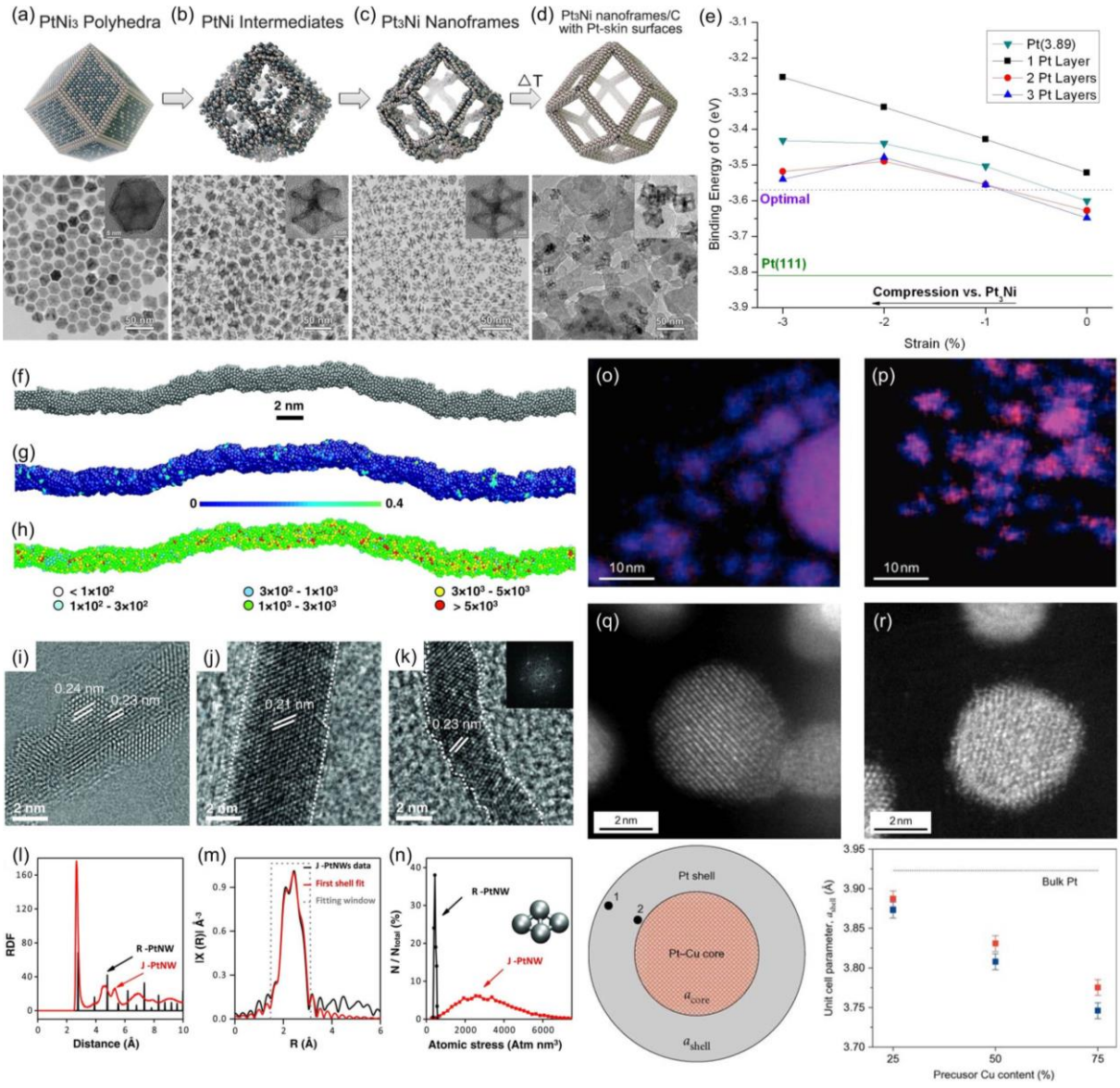

Figure 6. Porosity controlling induced strain. (a-d) Scheme and TEM images of the samples obtained at four representative stages during the evolution process. (e) Binding energy of O on Pt-terminated $Pt_3Ni(111)$ surfaces vs. compressive strain and number of Pt overlayers. Reproduced with permission.[26] Copyright 2014 American Association for the Advancement

of Science. (f) Scheme of a J-PtNW with an average diameter of ~2.2 nm and length of ~46 nm. (g) J-PtNW with colored atoms to show the five-fold index. (h) J-PtNW with colored atoms to show distribution of atomic stress (in atm·nm^3). HRTEM images (i to k) of the Pt/NiO core/shell nanowires, the PtNi alloy nanowires, and the J-PtNWs supported on carbon, respectively. (l) Pt-Pt radial distribution function (RDF) of the J-PtNW (red) compared with the peaks of the RDF for regular PtNW (black). (m) Pt L3 edge FT-EXAFS spectrum (black) and the corresponding first-shell least-squares fit (red) for the J-PtNWs. (n) Distribution of the absolute values of the average atomic stress on surface rhombi for the R-PtNWs (black) and the J-PtNWs (red). The inset shows the scheme of a rhombus. Reproduced with permission.[70] Copyright 2016 American Association for the Advancement of Science. High-resolution EDS (HR-EDS) elemental maps of (o) a $Pt_{25}Cu_{75}$ bimetallic nanoparticle alloy and of (p) the active electrocatalyst after Cu dealloying. HR-TEM images of (q) Pt-Cu alloy nanoparticle and (r) a typical Pt-Cu dealloyed nanoparticle. (s) Scheme of a simple two-phase structural model for the dealloyed state of a bimetallic particle. (t) Determination of α_{shell} for dealloyed Pt-Cu bimetallic particles vs. the alloy precursor Cu atomic composition at precursor annealing temperatures of 950 ºC (blue) and 800 ºC (red). Reproduced with permission.[41] Copyright 2010 Springer Nature.

Practically, the surface strain can be created simultaneously during catalyst synthesis. Stamenkovic and Yang *et al*. recently reported a highly active and robust electrocatalysts by exploiting the structural evolution of Pt-Ni bimetallic nanocrystals.[26] The starting material, crystalline $PtNi_3$ polyhedra, transforms in solution by interior erosion into Pt_3Ni nanoframes with 3D molecular accessible surfaces. The edges of the Pt-rich $PtNi_3$ polyhedra are maintained in the final Pt_3Ni nanoframes (**Figure 6**a-d). DFT simulations found that the optimal 2 to 3 monolayers of Pt create suitable strain (with respect to bulk Pt_3Ni) and thus favorable binding energy of O (Figure 6e).

Dealloying is another method to produce porosity and thus strain. Duan *et al*. used a thermal annealing process combined with electrochemical etching to transform solution-synthesized Pt/NiO core/shell nanowires to PtNi alloy nanowires and then jagged Pt nanowires (J-PtNWs, Figure 6f-h).[70] High-resolution TEM (HR-TEM) confirms the core/shell structure of Pt/NiO with a spacing of 0.24 nm for shell and a primary lattice spacing of 0.23 nm for core, corresponding to the (111) interplanar distance of face-centered cubic (fcc)NiO, and Pt (111) planes, respectively (Figure 6i). Upon annealing in Ar/H_2 mixture at 450 ˚C, the core/shell Pt/NiO converts to PtNi alloy nanowires (Figure 6j), which are further

transformed to J-PtNW by electrochemical leaching (Figure 6k). By conducting reactive molecular dynamics studies, the authors simulated the formation of J-PtNWs by leaching Ni atoms from initially $Pt_{15}Ni_{85}$ alloy nanowires. Moreover, a second moment approximation tight-binding potential was employed for final local optimization and prediction of Pt-Pt distances. J-PtNW exhibits a well-defined first-neighbor peak at about 2.70 Å (Figure 6l), about 2.2 to 2.5% shorter than those predicted for the R-PtNWs (2.76 Å) and the bulk Pt crystal (2.77 Å), which is well confirmed by the EXAFS analysis (Figure 6m). They also found that surface atoms in the J-PtNWs exhibit rather high values of Cauchy atomic stress times atomic volume (Figure 6n). This mechanical strain can decrease the binding energy of adsorbents on close-packed surfaces, which can make the surfaces more active, contributing to the activity enhancement. Strasser *et al*. dealloyed the Pt-Cu bimetallic nanoparticles to obtain Pt-rich shell with compressive strain.[41] As shown in Figure 6o, the elemental mapping image of $Pt_{25}Cu_{75}$ alloys implies the homogeneous distribution of Pt and Cu. In contrast, after dealloying, Cu is confined to the center of the majority of the dealloyed Pt-Cu nanoparticles, exhibiting a distinct Pt-enriched layer (blue) on the surfaces of the alloy Pt-Cu cores (Figure 6p). Aberration-corrected high-angle annular dark-field (HAADF) STEM images further confirm the change in the Pt and Cu distributions within the nanoparticles, from a uniform Pt-Cu alloy (Figure 6q) to a morphology suggestive of a core-shell structure (Figure 6r). They approximated the structure of the dealloyed nanoparticles by a simple two-phase core-shell model, as shown schematically in Figure 6s. By using the anomalous X-ray diffraction (AXRD) derived nanoparticle compositions and lattice-parameter data, along with their core-shell model, the lattice parameter α_{shell} can be determined (Figure 6t). Figure 6t shows that for all catalysts the lattice parameter of the Pt shell, α_{shell}, is smaller than that of pure Pt (dotted line) and so is strained compressively. They also found that the strain can be tuned by content of Cu in alloy precursors. Similarly, by simple two-step removing the active components in a

Pt/Ni/Al ternary alloy, Ding *et al*. obtained unique PtNi nanoporous structures with an open bicontinuous spongy morphology, which showed strain-enhanced electrocatalytic activity.[71]

3.1.2. Lattice Mismatch Induced Strain

When two or more metals or alloys with different lattice parameters are in direct contact, lattice mismatch is generated at the interface and in turn gives rise to lattice distortion (*i.e*., lattice strain) in each crystalline component. The effects of strain propagate through the crystal and decay further away from the interface due to relaxation around the interface. This can have an impact on the catalytic properties of the metal surface by modification of both the geometric and electronic structures. Numerous synthetic approaches have been reported to produce lattice mismatch such as alloying, doping, and epitaxial growth.

Alloying Induced Strain

Alloying noble metals with transition metals such as Ni and Co is an effective method to reduce the mass loading and/or improve the catalytic activities of noble metals catalysts by creating strain along with other effects. Chorkendorff *et al*. systematically studied eight Pt-lanthanide electrodes, Pt_5M, where M is lanthanum (La), cerium (Ce), samarium (Sm), gadolinium (Gd), terbium (Tb), dysprosium (Dy), thulium (Tm), or calcium (Ca).[72] They demonstrated how the lanthanide contraction can be used to control strain effects and tune the activity, stability, and reactivity of these materials. As shown in **Figure 7**a and 7b, most of the elements in the bulk Pt_5M alloy form a so-called kagome layer during electrocatalytic measurements within a nearest-neighbor Pt-Pt distance. The lattice parameter *a* and hence Pt-Pt distance decreased from left to right in the lanthanide series (Figure 7c). Calculations on strain-activity-reactivity relations suggest that Pt_5Tb, which is the most active electrocatalyst, should exhibit ~3% compression, approaching the optimum OH binding energy of the Sabatier volcano. By comparing activity data and voltammetric shift in H adsorption to the

DFT predictions, they conjectured that Pt-lanthanide alloys with a shorter Pt-Pt distance than Pt_5Tb form a more relaxed overlayer.

Abruna's group found intermetallic ordering of the PtCo alloy nanoparticles with a Pt-enriched shell for the particles prepared at higher annealing temperature. Importantly, the activity also followed lattice contraction in addition to degree of homogeneity. Since the surface contained at least a few monolayers of Pt, ligand and ensemble effects are significantly diminished, and so it is reasonable to attribute the activity increase to compressive strain of Pt surface atoms.[73] A similar finding was discovered by Zhu's group.[74] Strain maps were generated from HRTEM lattice images of cuboctahedral uniform PtFe alloys nanoparticles (Figure 7d and 7e) and they found the lattice contraction relative to Pt is generally quite uniform (Figure 7f).

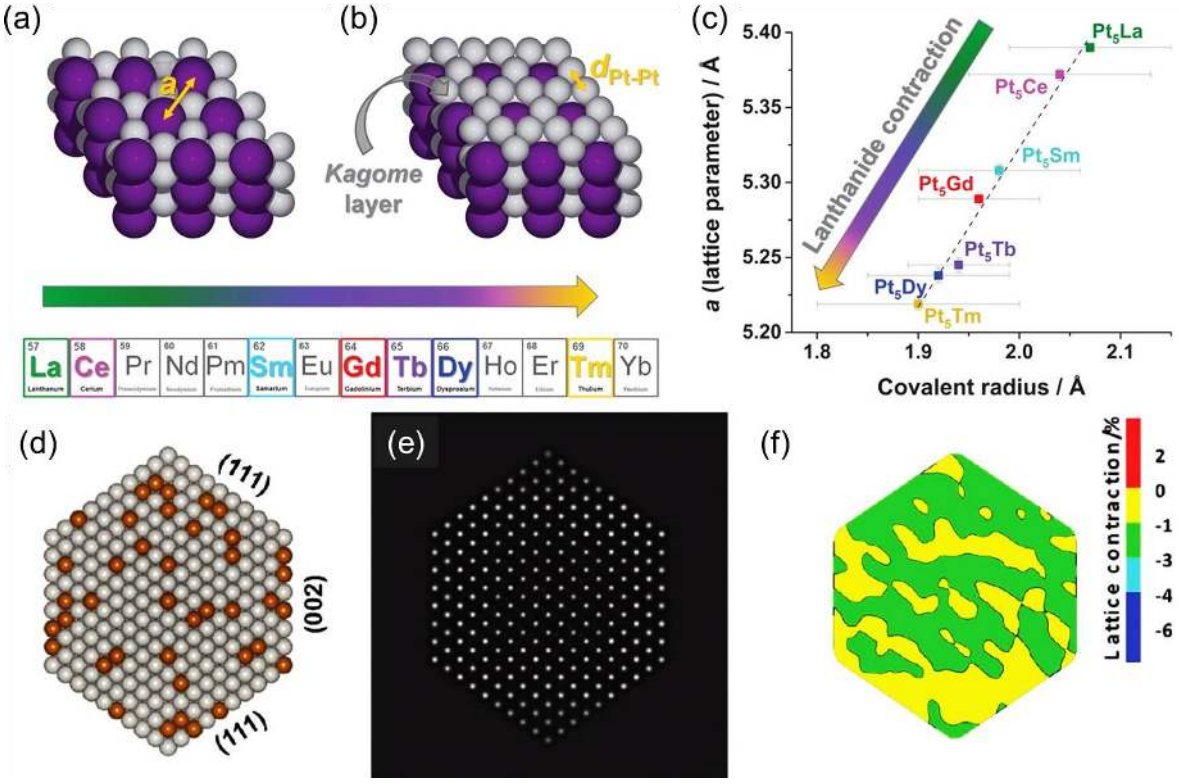

Figure 7. Alloying induced strain. (a and b) Schematic view of the bulk structure of a Pt_5M showing Pt_5Tb terminated by (a) a Pt and Tb intermixed layer and (b) a Pt kagome layer. Purple spheres represent Tb atoms, and gray spheres represent Pt atoms. (c) Relation between the lattice parameter *a* of Pt_5M measured by XRD and the covalent radius of the lanthanide atoms. Reprinted with permission.[72] Copyright 2016 American Association for the

Advancement of Science. (d) Structural model of cuboctahedral uniform alloy nanoparticles. (e) Simulated HRTEM image. (f) The map of the lattice contraction relative to bulk Pt. Reproduced with permission.[74] Copyright 2012 American Chemical Society.

Epitaxial Growth Induced Strain

Heterogeneous epitaxy has long been used in gas-phase deposition to prepare functional heterostructures or junctions. For example, Xia's group demonstrated epitaxial growth of Pt layers on Pd icosahedra to form Pd@Pt_{nL} core-shell icosahedra with well-controlled shell thickness (**Figure 8**a-d).[75] Owing to the lateral confinement imposed by twin boundaries, the Pt overlayers could only relax along the direction normal to the surface to generate a corrugated structure with compressive strain. Similar result was also reported in Au-Pt core-shell star-shaped decahedra (Figure 8e-g).[76] By using hexagonal-close-packed (hcp) Au squaresheets (AuSSs) as templates, Zhang's group synthesized the ultrathin face-centered-cubic (fcc)Au@Pt rhombic nanoplates via the epitaxial growth.[77] A number of stacking faults and internal twinning were generated; and hence strain was produced. Subsequently, they extent this method to other substrates such as 4H Au nanoribbons.[78] Assisted by galvanic replacement, these alloy shells with novel 4H hexagonal phase, *i.e.*, PdAg, PtAg, and PtPdAg, were successfully grown on the 4H/fcc Au core via epitaxial growth (Figure 8h).[79]

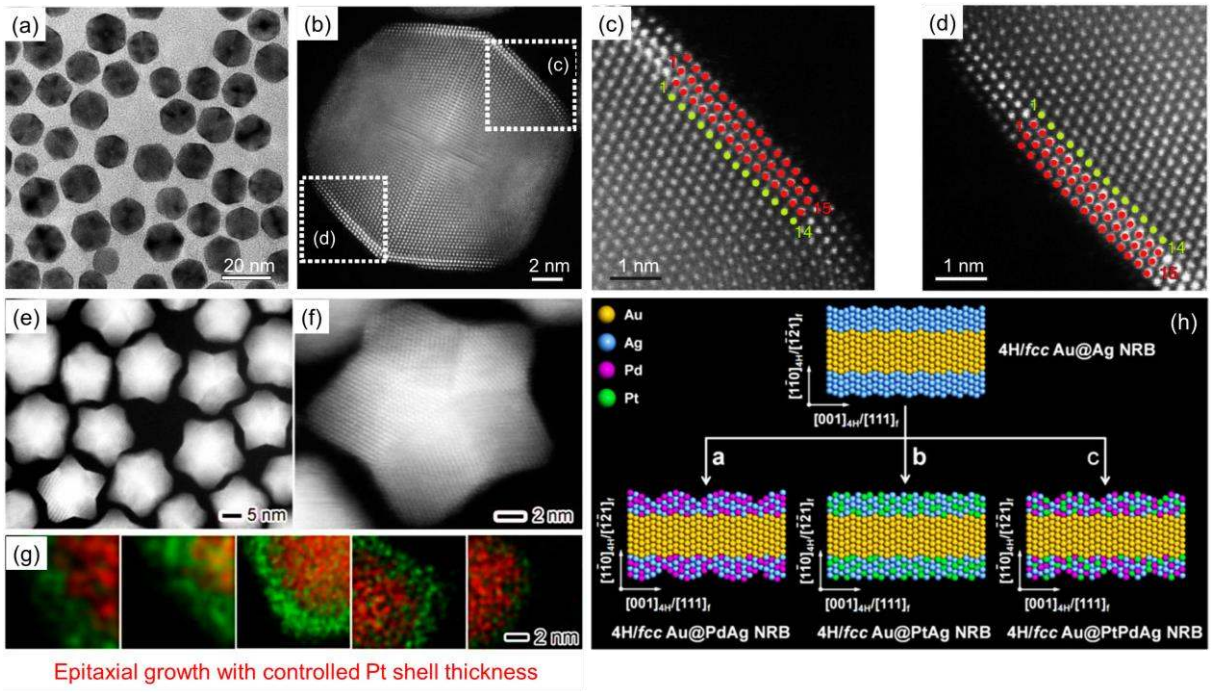

Figure 8. Epitaxial growth induced strain. (a) TEM images and (b-d) HAADF-STEM image of the Pd@$Pt_{2.7L}$ icosahedra. Reproduced with permission.[75] Copyright 2012 Springer Nature. (e, f) HAADF-STEM image of Au-Pt star-shaped decahedra at different magnifications. (g) Elemental mapping of Au-Pt star-shaped decahedra with controlled shell thickness. Reproduced with permission. [76] Copyright 2015 American Chemical Society. (h) Schematic of 4H/fcc Au@PdAg, Au@PtAg, and Au@PtPdAg core-shell NRBs from 4H/fcc bimetallic Au@Ag core-shell NRBs. Reproduced with permission.[79] Copyright 2016 American Chemical Society.

3.2. Two-Dimensional Nanocatalysts

Two-dimensional TMDs have been extensively studied as catalysts for various chemical processes, ranging from commercial hydrodesulfurization for petroleum industrial [80-82] to water electrolysis for renewable energy.[83, 84] As a representative of TMD family, MoS_2 has been intensively investigated as a catalyst for various catalytic reactions.[85-92] As the first experimentally isolated monolayer semiconductor, strain-induced physical properties modulation of MoS_2 have been intensively studied.[93-97] In contrast, its strain-modulated chemical/electrochemical/catalytic properties remain largely underexplored. This is mainly caused by the constraints of most existing strain techniques that are more suitable for small area characterization. In this section, we will review the strain techniques for 2D materials, hoping to introduce all available strain methods to date. Then, we will propose new strain

methods that could overcome the limitation of the state-of-the-art strain methods, and thus are suitable for fundamental reaction mechanism study or practical applications for water splitting reactions and beyond.

2D materials have inherent advantages on leveraging strain engineering for modulation of their intrinsic physical or chemical properties. Firstly, 2D materials are extremely flexible owing to their atomic thickness. Secondly, 2D materials are extraordinarily strong due to the very stable in-plane atomic bonds. For instance, 2D metal graphene has a breaking strength of 42 N m^{-1}, and can sustain up to 25% elastic strain.[98] 2D semiconductor MoS_2 has a breaking strength up to 18 N m^{-1}, and can sustain 11% elastic strain.[99, 100] Thirdly, the electronic structures of most 2D materials are sensitive to strain. Properly designed strain is proposed to open significant bandgap in semimetallic graphene.[101] Biaxial tensile strain reduces the electronic bandgap of MoS_2 at the rate of 200 meV per %. Biaxial compressive strain also readily reduces the electronic bandgap of MoS_2.[102-104] In fact, about 9% biaxial tensile or 14% compressive strain changes MoS_2 from semiconductor to metal with greatly enhanced conductivity.[102] Similar findings apply to most of TMDs, with different bandgap reduction rate on strain in distinct TMDs.[103] Therefore, intensive investigations of the influence of strain on the electronic structure of 2D materials have been conducted both theoretically and experimentally.[102, 103, 105-114] For simplicity, we categorize these works into two groups: strained TMDs on flexible substrate (flexible substrate induced strain) and that on hard substrate (rigid substrate induced strain). The rationale behind is that it is facile to induce strain using flexible substrates, but the method is not scalable; and thus it is meant for fundamental study. In contrast, rigid substrate induced strain is difficult to implement, however it is more scalable; and thus it could be employed in practical device.

3.2.1. Flexible Substrate Induced Strain

Since the ultrathin 2D materials behaves essentially like a thin plastic wrap, it could be easily attached onto a flexible substrate, and then get strained by deforming the substrate such as polyethylene terephthalate (PET), polymethyl methacrylate (PMMA) and polydimethylsiloxane (PDMS) *etc*. The early works on strained graphene and MoS_2 were carried out using these flexible substrates. For instance, graphene can be controllably and reproducibly strained by using two- or four-point bending setups, as shown in **Figure 9**, where *F* shows the direction of the applied forces to deform the substrate.[105] PET and acrylic (Perspex) films were used as the substrates for two- (Figure 9a) and four-point (Figure 9b) bending experiments. The substrates were spun coated with SU8 photoresist of chosen thickness (~400 nm) that enables visible monolayer graphene on the substrate. Graphene layers were prepared by mechanical cleavage directly onto the substrate. This mechanical compression process results in the strong van der Waals interaction between graphene and the substrate. This in turn ensures the synchronized deformation of graphene layer when the substrate is deformed. Since the area of the graphene layer is 1,000~10,000 times smaller than the substrate, the strain in graphene caused by stretching the substrate is almost uniformly generated. Though this method has been employed widely for straining 2D materials, it has four apparent limitations (1) the 2D layer may slip with respect to the substrate during bending and thus a calibration of strain is necessary, (2) the strain in 2D layer may not be uniform if the adhesion between graphene and substrate is nonuniform or the substrate deformation is nonuniform, (3) the strain along *y* axis that is perpendicular to the substrate deformation direction is unknown, and (4) the graphene layer may complete peel off from the substrate due to insufficient adhesion force (*i.e*., the van der Waals force) at large strain. These issues can be partially addressed by adding metal clamp onto the graphene flake, as presented in Figure 9c.[106] The uniaxial tensile strain was applied to graphene upon bending the PDMS substrate perpendicular to the titanium clamping strips. One can see that the metal

strips deformed, indicating that the strain in graphene is smaller than that in PDMS, as shown in Figure 9d. With optical microscope, the change in gap between metal strips (Δl) can be measured and the strain along x axis was calculated by $\varepsilon = \Delta l/L$, where L is the original gap length. The strain along y axis could be calculated under the assumption of stress-free boundary condition along the lateral edges of the graphene. The calculated uniform strain area is labeled by dotted line in Figure 9d, suggesting the nonuniform strain distribution in graphene. With such a calibration combining theory and experiment, the strain distribution in graphene was obtained with much better accuracy.

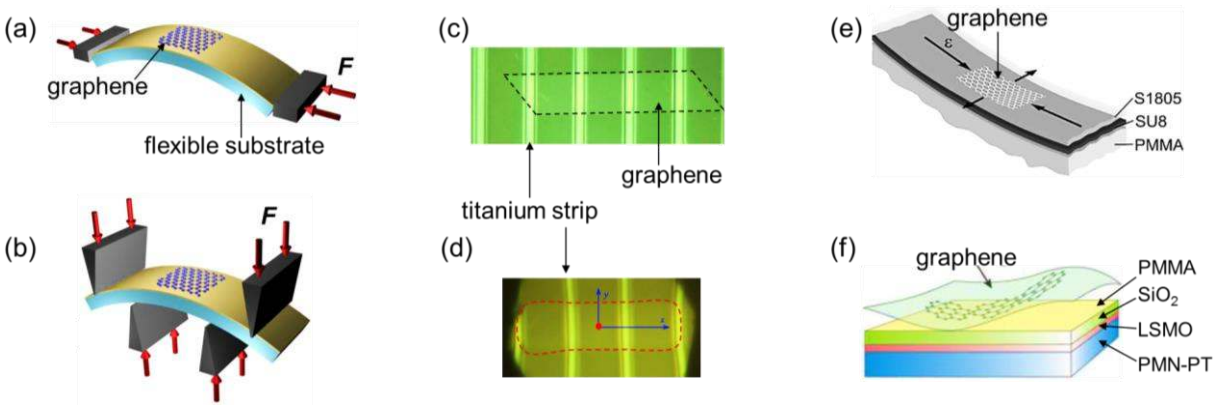

Figure 9. Strain 2D materials on flexible substrate. (a) Two-point bending of PET substrate and (b) four-point bending of acrylic (Perspex) substrate to introduce tensile strain in graphene directly exfoliated onto the substrate. Reproduced with permission.[105] Copyright 2009 American Physical Society. (c) Fixed graphene on PDMS by titanium clamping strip. (d) Optical microscope image of the fixed graphene under tension along x axis. Serious deformation of titanium strip was observed. Red dotted labels the simulated uniform tensile strain area. Reproduced with permission.[106] Copyright 2009 National Academy of Sciences of the United States of America. (e) Sandwiched trilayer film (SU8-graphene-S1805) on PMMA beam. When the two ends of the beam bend upwards, compressive strain was applied to graphene.[107] (f) Biaxial strained graphene on PMN-PT substrate. Reproduced with permission.[108] Copyright 2010 American Chemical Society.

A slight modification of the method allows one to apply compressive strain to graphene, as displayed in Figure 9e.[107, 115] The graphene layer was sandwiched between two polymeric layers of SU8 and S1850, and the sandwich trilayer film was placed onto PMMA beam. The deflection was measured accurately using a dial gauge micrometer attached to the top surface

of the beam. This method could apply both tensile and compressive strain up to 1.5%. Piezoelectric materials such as $[Pb(Mg_{1/3}Nb_{2/3})O_3]_{0.72}$-$[PbTiO_3]_{0.28}$ (PMN-PT) substrate could generate stress when an external electric field is applied, because the external electric field can expand or shrink the piezoelectric materials controllably and reversibly. This makes the piezoelectric substrate "flexible" under an external electric field. As shown in Figure 9f, both biaxial tensile and compressive strains can be applied to a graphene layer when it is placed onto a PMN-PT substrate.[108] The substrate consisted of a 40-nm-thick epitaxial layer of $La_{0.7}Sr_{0.3}MnO_3$ (LSMO) grown on 300-μm-thick PMN-PT substrate. A 1 μm-thick SiO_2 layer was deposited onto LSMO layer, and then capped by 60-nm-thick PMMA film. A graphene layer on scotch tape by mechanical cleavage was placed onto the substrate followed by a heating process at 120°C for 5 min. The PMMA was cured and harden, and fixed the graphene layer onto the substrate. When the substrate deformed under electric field, the graphene layer was strained biaxially. The disadvantage of this method is that only limited amount of strain (~0.1%) can be applied at the cost of very high applied voltages (~1000 V); thus it is difficult to implement.

3.2.2. Rigid Substrate Induced Strain

One can see that all of the aforementioned strain methods leverage flexible substrates, which are not suitable for practical devices that usually have rigid substrates. **Figure 10** summarizes the strain methods of 2D materials on rigid substrates. Bunch *et al.* deposited a monolayer MoS_2 grown by CVD onto a SiO_2 substrate with microcavities (the grey circles in Figure 10a).[109] The microcavities are circular holes with diameters of 5 μm and depths ranging from sub-μm to a few micrometers. The sample was placed in a high pressure (P_0) chamber for sufficient duration to allow the gas (could be nitrogen, argon, hydrogen or helium) to leak into the cavity that originally contains air with pressure of 1 atm (P_{int} = 1 atm). When the internal pressure inside cavity reached that of P_0, *i.e.*, $P_{int} = P_0$, the sample was taken out

from chamber. As such, the pressure difference between air ambient (*i.e.*, the external pressure outside the cavity P_{ext}) and the internal pressure, *i.e.*, P_0 - P_{ext}, would inflate the MoS_2 layer to form a balloon (see Figure 10b for the AFM image of a MoS_2 balloon). Similar approaches have been employed to strain other 2D materials.[116, 117] Coating of 2D materials onto nanostructured substrate could cause local strain in 2D materials. Dettlaff-Weglikowska *et al.* placed a graphene on a periodic grid of hydrogen silsesquioxane (HSQ) resist defined by electron-beam lithography, as illustrated in Figure 10c.[110] Owing to the tiny feature (~10 nm) and uniform period, periodical local strain could be introduced into graphene. Steele *et al.* created very local strain in MoS_2 using pre-stretched elastomeric substrate (Gel-Film).[111] The elastomeric substrate was stretched by 100%, and then the MoS_2 flakes were directly exfoliated onto the elastomeric substrate. When the tension in the substrate was released, wrinkles in the MoS_2 layers were generated due to buckling-induced delamination, as shown in Figure 10d. Uniaxial tensile strain was introduced into MoS_2 wrinkles due to the serious local bending.

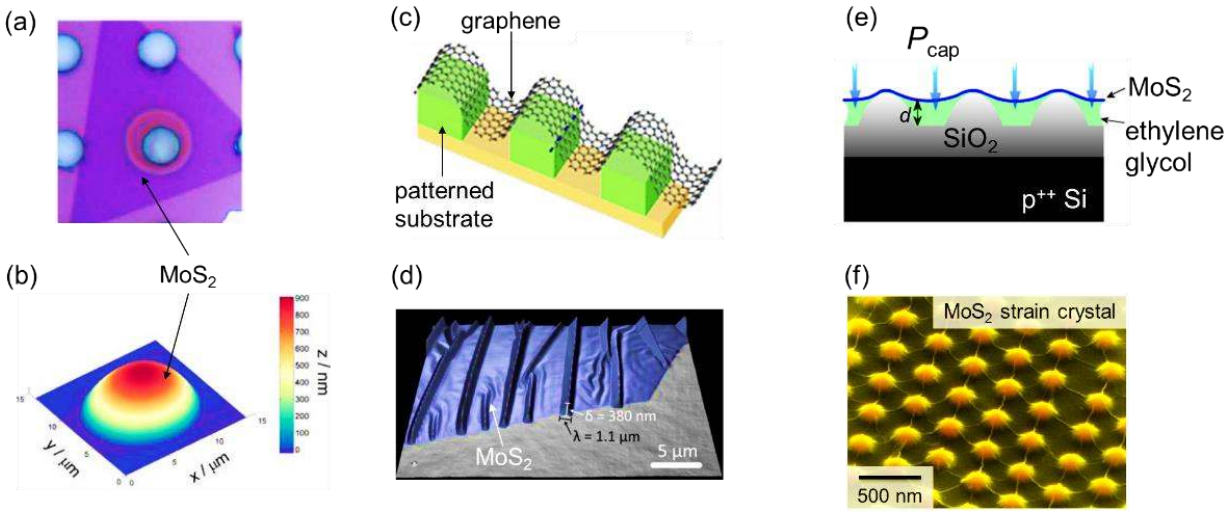

Figure 10. Strain 2D materials on rigid substrate. (a) An optical image of a triangular MoS_2 flake covering SiO_2 with pre-patterned circular microcavities (diameter ~ 5 µm and depth of a couple of µm). (b) An AFM image of a MoS_2 bubble. Inset: color bar of height. Reproduced with permission.[109] Copyright 2017 American Chemical Society. (c) Schematic of strained graphene on periodic grid nanostructure of HSQ (10 nm in both height and width).[110] (d) Nanowrinkles of MoS_2 formed on pre-strained elastomeric substrate. Reproduced with

permission.[111] Copyright 2013 American Chemical Society. (e) Schematic straining process utilizing capillary pressure. The thin MoS_2 layer (blue line) is placed above SiO_2 nanocones patterned on Si substrate. Ethylene glycol (green color) is filled between MoS_2 layer and substrate. (f) Tilted SEM image of a strain-textured MoS_2 monolayer on SiO_2 nanocone array. Reproduced with permission.[57] Copyright 2015 Springer Nature.

Straining 2D materials on nanostructured substrate appears to be a scalable method. We have developed such a technique and the idea is illustrated Figure 10e,[57] where the cross-section schematic of a sample is shown. The method leverages capillary pressure to pull the MoS_2 monolayer against the substrate. When a MoS_2 sheet (blue line) is transferred onto the nanostructured substrate [silicon dioxide (SiO_2) nanocone array (grey color) pre-patterned on SiO_2/Si substrate], there are gaps between relaxed MoS_2 film and the substrate (valleys between SiO_2 nanocones). A solvent ethylene glycol is then filled into these gaps (green color area) in vacuum chamber, which removes the pre-trapped air in the gaps. When the solvent evaporates in air ambient, the generated capillary pressure P_{cap} presses the MoS_2 sheet against the substrate. As P_{cap} is inversely proportional to the gap height d, the capillary force becomes tremendous when d is decreasing. Eventually, the MoS_2 sheet conformally coats onto the substrate when the solvent dries out. Then, the MoS_2 sheet stays on substrate due to van der Waals interaction. Owing the enlarged surface area of MoS_2 after straining process, elastic tensile strain is incorporated into MoS_2 lattice and its spatial distribution depends on the nanostructure, as demonstrated in Figure 10f, where the top view of a strain-textured MoS_2 monolayer is seen. The tiny wrinkles (~1 nm in height) between adjacent cones proved the severe distortion of MoS_2 film. The local strain was measured by scanning tunneling microscopy (STM) to be as high as 2.85% (biaxial tensile strain) on the tip of the nanocones.

Other nanostructured substrates have been employed to strain 2D materials as well. Mason *et al.* strained graphene on mesoscale pyramid arrays.[112] A PDMS substrate with pyramid array surface was made by molding process, where the polycarbonate mold was made by nanoindentation. A CVD graphene layer was transferred onto the pyramid array and

conformally coated onto the substrate if the aspect ratio (pyramid spacing: pyramid height) meets certain requirements that also depend on the substrate surface condition. Reserbat-Plantey *et al.* transferred a CVD graphene layer onto SiO_2 nanopillar array, and produced many tiny graphene wrinkles where graphene could have significant local strain.[113, 118] Other strain methods that have been less widely employed include hydrostatic pressure using diamond anvil cell [114] or nanoindentation using atomic force microscopy tip.[98-100] Another notable method is to create strain by lattice mismatch at 2D material heterojunctions or homojunctions, which will be detailed in the next session.

4. Strain-Promoted Hydrogen Evolution Reaction

4.1. Non-Two-Dimensional Nanocatalysts

Strain engineering has shown promise to further improve the HER performance of those diverse catalysts including noble metals and nonprecious materials. For example, Stamenkovic and Yang *et al*. recently obtained Pt_3Ni nanoframes.[26] The three-dimensional molecular accessible surfaces that can improve the usage of surface Pt atoms. Besides, the strain effect has been proved to be beneficial for the enhanced HER under alkaline solution (0.1 M KOH); resulting in better activity than that of commercial carbon supported Pt nanoparticles (Pt/C) and solid PtNi/C (**Figure 11**a-c). Recently, Zhang *et al*. reported the Au@PdAg nanoribbons (NRBs) with a rough dendritic surface (Figure 11d-l).[79] This dendritic nanostructure would result in epitaxial strain and lower coordinated atoms, both of which can alter bonding intensity of catalyst and reactants. Electrochemical measurements demonstrated that the Au@PdAg NRBs exhibit much higher electrocatalytic activity toward HER compared to that of Pd black, which is even comparable with that of Pt black. As shown in Figure 11m, the onset potentials of Au@PdAg NRBs, commercial Pd black, and Pt black are 2.0, 85.0, and 0.5 mV, respectively. Also, the overpotentials at 10 mA cm^{-2} are 26.2, 135.6, and 16.5 mV, respectively. Note that both the onset potential and overpotential for Au@

PdAg NRBs are quite close to those for the Pt black, implying their comparable HER activity. In addition, the Au@ PdAg NRBs also show robust stability; no obvious shift of the polarization curve is observed after 10 000 potential cycles from +0.448 to -0.152 V (vs. RHE) in 0.5 M H_2SO_4 solution (Figure 11n).

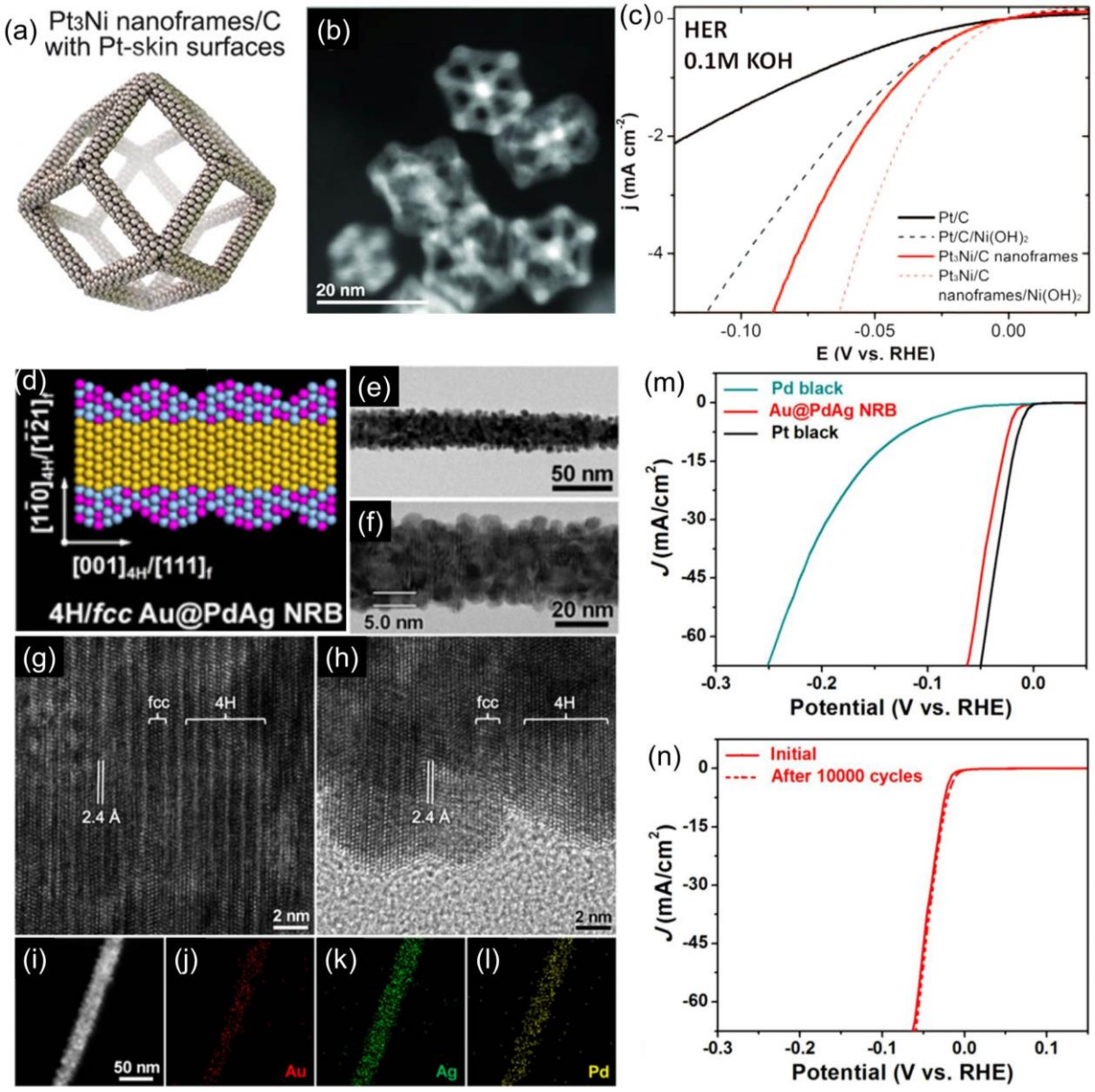

Figure 11. Effect of alloying-induced strain on HER activities of metal alloys. (a) Scheme and (b) STEM images of Pt_3Ni nanoframes. (c) Polarization curves of Pt_3Ni nanoframes along with Pt/C and solid PtNi/C control samples for HER in 0.1 M KOH. Reproduced with permission.[26] Copyright 2014 American Association for the Advancement of Science. (d) Scheme, (e-h) TEM images at different magnifications, (i-l) STEM and elemental mapping images of 4H/fcc Au@PdAg core-shell NRBs from 4H/fcc bimetallic Au@Ag core-shell NRBs. (m) Polarization curves of 4H/fcc trimetallic Au@PdAg NRBs, Pd black and Pt black.

Linear sweep voltammetry was conducted in 0.5 M H_2SO_4 solution at scan rate of 5.0 mV s^{-1}. (n) Durability test of 4H/fcc trimetallic Au@PdAg NRBs. Reproduced with permission.[79] Copyright 2016 American Chemical Society.

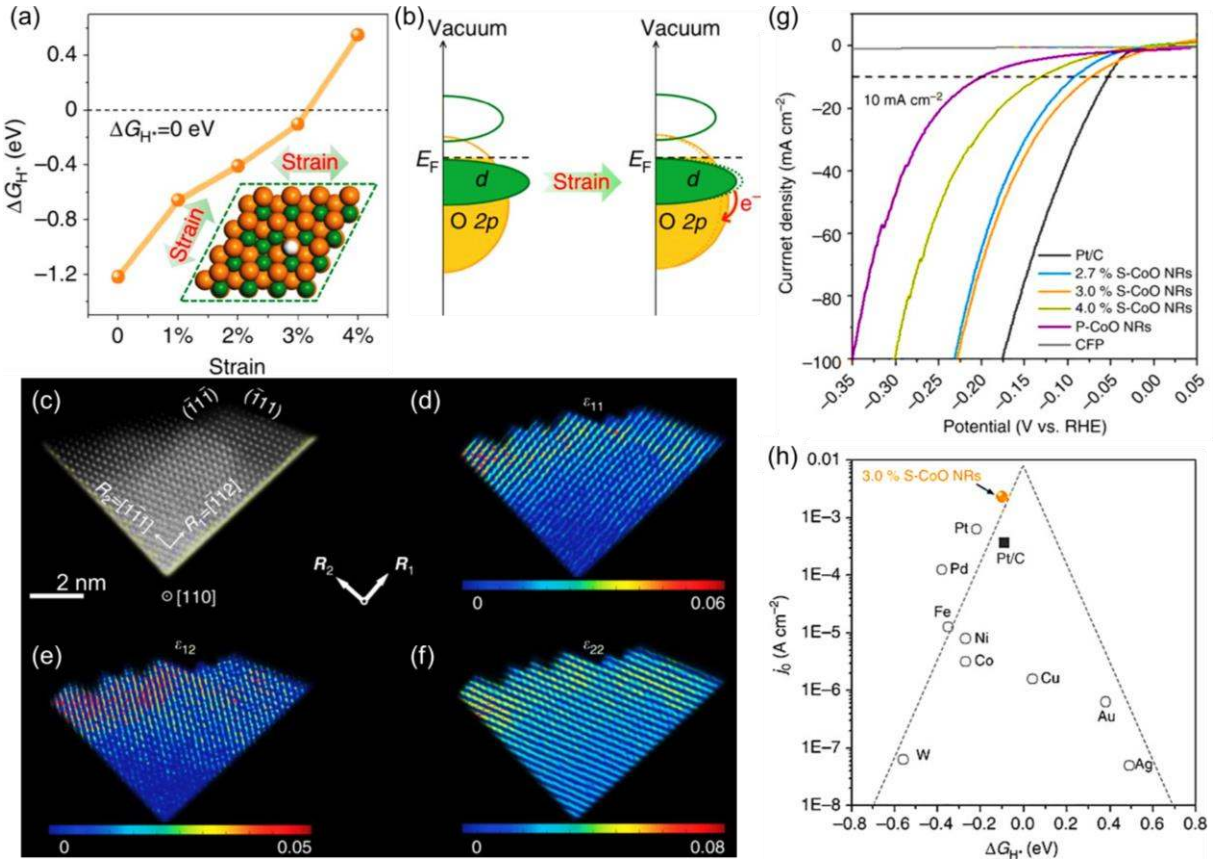

Figure 12. Effects of oxygen vacancy-induced strain on HER performance of transition-metal oxide CoO. (a) Hydrogen adsorption free energy, ΔG_{H^*}, vs. tensile strain for the CoO {111}-Ov surface. (b) Schematic illustration of the effect of strain on the electronic structure of {111}-Ov surface of CoO. (c) Atomic resolution HADDF-STEM image of two adjacent nano-sawtooths enclosed with {111} nanofacets, indicating the lattice vectors R_1 and R_2 used as a reference for the strain analysis. (d-f) Contour plots of the strain component ε_{11} (d), ε_{12} (e), and ε_{22} (f) relative to the reference values. (g) Linear sweep voltammetry (LSV) curves of S-CoO NRs with different tensile strains, P-CoO NRs, commercial Pt/C catalysts, and CFP substrate recorded in 1 M KOH solution with iR-correction. (h) Volcano plots of j_0 measured in alkaline solution as a function of the ΔG_{H^*} for diverse catalysts. Reproduced with permission.[119] Copyright 2017 Springer Nature.

Besides these noble-metals-based HER electrocatalysts, Qiao's group recently observed that the strain engineering is also powerful to improve the HER performance of transition-metal oxide (CoO) catalysts, which are traditionally considered as HER-inactive materials.[119] When tensile strain is exerted on O-vacancy-rich {111}-O surface ({111}-Ov surface, with 11.1% surface O-vacancies), H* adsorption is continuously weakened with increasing

magnitude of the applied strain (**Figure 12**a). Surprisingly, 3.0% strain resulted in ΔG_{H^*} of -0.10 eV, which is close to the optimal value of ΔG_{H^*} = 0 eV. Additionally, the tensile strain upshifts the O 2p-band of CoO, resulting in greater covalence of the Co-O bond (Figure 12b). It's suggested the surface O can bind more strongly to its neighboring Co atoms and thus weaken its capability of withdrawing electrons from the adsorbing H atom. To verify the above theoretical predictions, they attained CoO nanomaterials with strained and O-vacancy enriched surfaces by using cation exchange methodology. Figure 12c demonstrates an HADDF-STEM image of two adjacent nano-sawtooth planes. The lattice strain component ε_{11} (in {111} plane) and ε_{22} (perpendicular to {111} plane) associated with the expansion/contraction of the respective lattice vectors R_1 and R_2 are presented in Figure 12d-f. The values of ε_{11}, ε_{12}, and ε_{22} are approximately zero in the inner part of the NR, while they gradually increase to large positive values on the outermost surface of the nano-sawtooth structure, indicating biaxial-induced strain on this surface. As shown in Figure 12g, the polycrystalline CoO NRs (P-CoO NRs) need large overpotential at 10 mA cm^{-2} and thus low HER activity. In contrast, the overpotential at 10 mA cm^{-2} of strained CoO NRs (S-CoO NRs) is largely decreased. Specifically, the 3.0% S-CoO NRs show superior activity, even compare favorably to that of Pt/C catalysts. Moreover, the activity of the 3.0% S-CoO NRs in 1 M KOH solution, assessed on the basis of both ΔG_{H^*} and j_0, surpasses those of the common noble- and transition- metals (Figure 12h).

4.2. Two-Dimensional Nanocatalysts

Most aforementioned methods generate strains in small-area 2D catalysts, insufficient for lab-scale electrochemical devices that usually have geometric area of square centimeters or larger. Thus, these strain methods have attracted much less attention in the field of electrochemistry. Nevertheless, careful designs of the reaction cells or catalyst systems could leverage these strain methods. For instance, the advances of nanofabrication make it possible

to study chemical reactions in microscale reaction cells.[120, 121] We will discuss a few representative examples that clearly demonstrate strain effects in 2D HER catalysts in this session. Afterward, we will propose a few designs of reaction cell and catalyst structures that are able to utilize elastic strain.

4.2.1. Lattice Mismatch Induced Strain

Similar to nanoparticles, lattice mismatch can also induce significant strain in 2D materials. TMD has a big family of dozens of members that have distinct lattice parameters. Lattice mismatch can cause local strain at heterojunctions, homojunctions or defective sites of TMD heterostructures.[122-127] Such lattice mismatch induced strain is beneficial to optimize the hydrogen adsorption free energy, and thus enhance the hydrogen evaluation reactions.[123-126] Chhowalla M. *et al*. have detailed the impact of the strain caused by 1*T*-phase tungsten disulfide (WS_2) in the matrix of 2*H*-phase WS_2.[125] The sample was prepared by chemical exfoliation of bulk 2*H*-phase WS_2 powder, where 1*T*-phase lattice was created during intercalation, forming plenty of homojunctions. The lattice mismatch between 1*T*- and 2*H*-phase WS_2 results in distorted 1*T* superlattice phase, as shown in HAADF-STEM image (**Figure 13**a), where the corresponding stress tensor map of such a distorted superlattice is inserted. Both tensile and compressive stresses are seen. In the highlighted zigzag chain superlattice regions, two different W-W atom distances, 2.7 Å and 3.3 Å, are observed. Compared to that of 3.15 Å for 2*H* phase, these W-W atom distances indicate compressive and tensile strain, respectively. The overall change of lattice parameter in the sample is ~3%.

Since the 1*T* phase is metastable, it could be converted to 2*H* phase by thermal annealing. Thus, the concentration of 1*T* phase could be varied by changing the annealing temperature. Higher annealing temperature should result in less 1*T* phase and thus poorer HER activity. The intrinsic HER activity of the catalyst is quantified by turnover frequency (*TOF*), *i.e*., number of H_2 molecules generated per second per site, where the active site density is

measured by the copper underpotential deposition method.[128] Figure 13b shows the intrinsic HER activity (*TOF*) of the as-prepared 1*T*-phase WS_2 and annealed 1*T*-phase WS_2 (at 300 ºC), along with the bulk 2*H*-phase WS_2. Indeed, the HER activity significantly decreases when the sample is annealed. A detailed dependence of the total HER activity (exchange current density) on 1*T*-phase percentage is presented in Figure 13c. The linear dependence of total HER activity on the 1*T*-phase concentration suggests that the strained 1*T* phase is much more active than 2*H* phase for hydrogen evolution. The authors performed theoretically study to obtain possible mechanisms for the high HER activity using similar DFT framework discussed earlier. It is found that strain could significantly influence the free energy of hydrogen adsorption on the surface of distorted 1*T*-phase WS_2, as shown in Figure 13d. 2.7% tensile strain could reduce the free energy from 0.28 eV to 0, *i.e.*, the thermoneutral condition. The combined experimental and theoretical studies strongly suggest the significant contribution of elastic strain in promoting HER activity of WS_2 catalyst. Similar to nanoparticle and nanowire catalysts, doping could also introduce significant amount of lattice mismatch and thus strain to promote HER.[129]

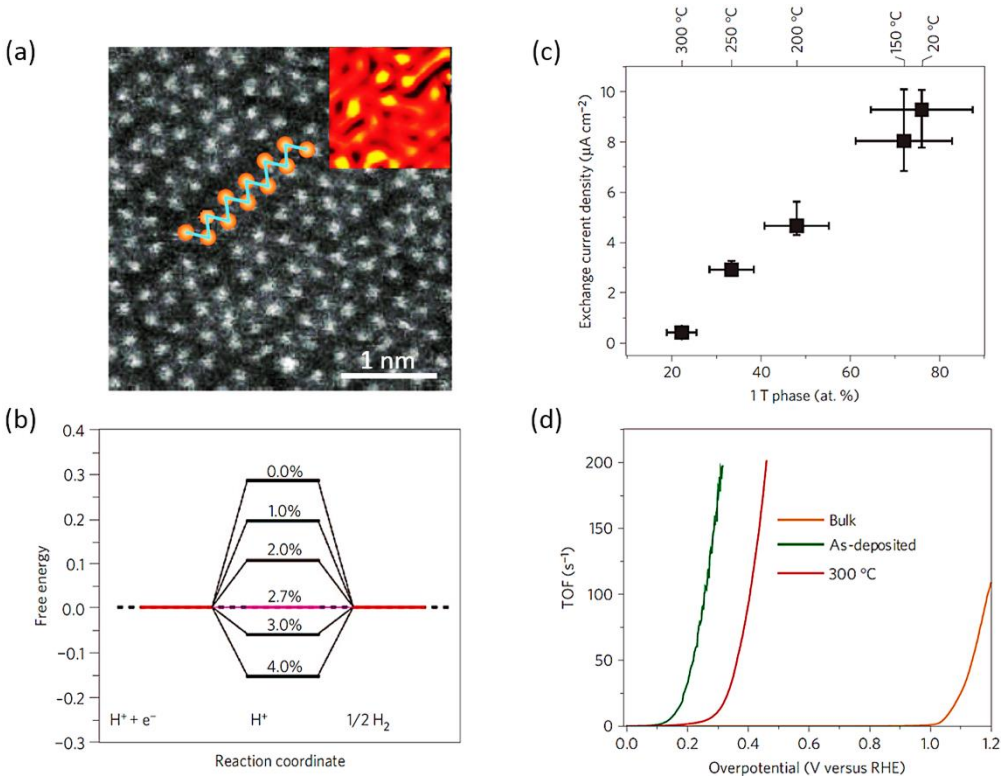

Figure 13. Lattice mismatch induced strain for enhanced HER activity. (a) TEM image of chemically exfoliated WS_2. Inset: stress tensor map (7.45 × 7.45 nm^2) of distorted 1*T* superlattice phase calculated from TEM images. A schematic atom arrangement is overlaid on the TEM image, where the orange circles represent W atoms. Scale bar represents 1 nm. (b) The calculated free energy for hydrogen evolution at equilibrium with tensile strain in 1*T*-phase WS_2. (c) Exchange current density (total HER activity) as a function of 1*T* phase concentration varied by annealing the sample in inert atmosphere (the annealing temperature is labelled on top *x* axis). (d) TOF versus the overpotential of bulk 2*H*-phase WS_2 (rightmost curve), as-prepared chemically exfoliated 1*T*-phase WS_2 (leftmost curve), and annealed 1*T*-phase WS_2 at 300 ºC (middle curve). Reproduced with permission.[125] Copyright 2013 Springer Nature.

4.2.2. Bending Substrate Induced Strain

Bending the substrate to introduce strain into 2D materials is a popular method for study of the physical properties of materials (see Figure 9 for summary); but it has attracted much less attention for investigation of chemical properties of materials under strain. Nevertheless, there are still a few attempts to employ this method to enhance HER activity of 2D catalysts, as illustrated in **Figure 14**. Baik *et al*. printed vacuum-filtered MoS_2 film made by chemical exfoliation onto Ag-coated PET substrate.[130] By bending the PET substrate, up to 0.02% estimated tensile strain could be applied to the MoS_2 film deposited on the substrate. The current density increases from 41 to 48 mA cm^{-2} when tensile strain is increased from 0 to 0.02%, as presented in Figure 14b. However, limited performance enhancement could be obtained due to the limited amount of strain that is able to achieve using this method.

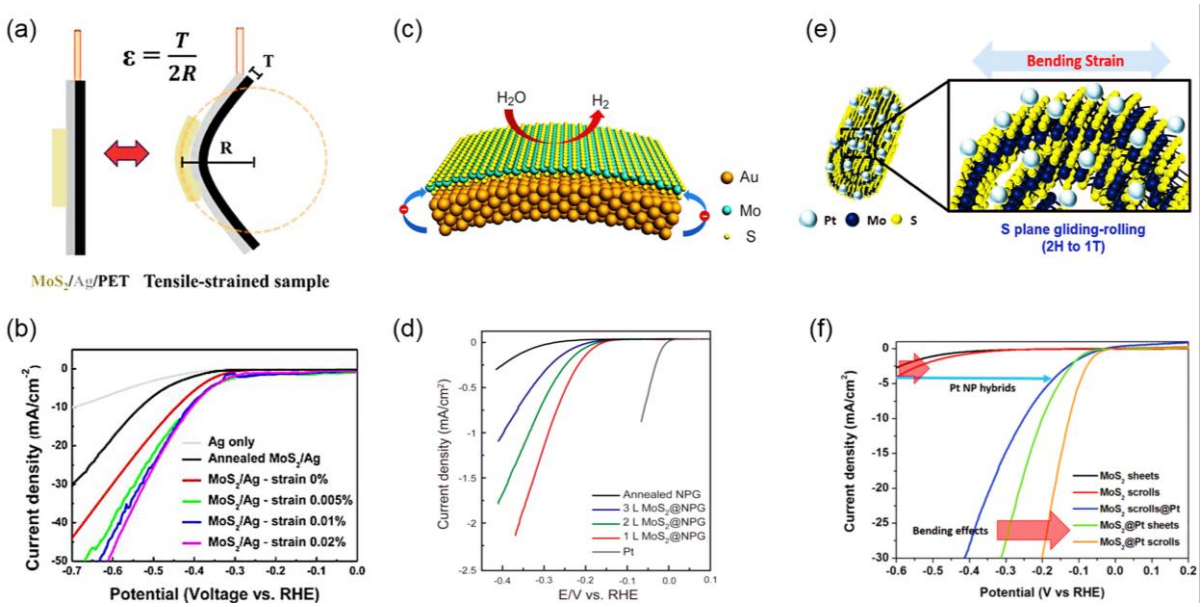

Figure 14. Bending substrate induced strain for enhanced HER activity. (a) Schematic strain method by bending the Ag/PET substrate, where R is the bending radius, T is the PET substrate thickness and $\varepsilon = T/2R$ is the estimated strain magnitude. (b) Strain-dependent polarization curves. Reproduced with permission.[130] Copyright 2014 American Chemical Society. (c) Schematic HER reaction catalyzed by atomically strained MoS_2 on curved gold surface. (d) Polarization curves of Pt, pure NPG, and MoS_2@NPG. Reproduced with permission.[131] Copyright 2014 Wiley-VCH. (e) Schematic atomic structure of MoS_2@Pt scrolls with bending strain. (f) The polarization curves for MoS_2 sheet and scroll electrodes before and after the Pt hybrid process. The arrows highlight the strain effects caused by scrolling MoS_2 sheets. Reproduced with permission.[132] Copyright 2017 Royal Society of Chemistry.

Chen *et al.* fabricated strained MoS_2 film by directly growing monolayer MoS_2 film on the curved internal surface of a mesoporous gold (NPG) substrate, as illustrated in Figure 14c.[131] Owing to the strong coupling between MoS_2 layer and gold substrate surface, the MoS_2 layer was grown following the curved gold surface, and then got strained at atomic level. Side view HAADF-STEM image shows that the MoS_2 monolayer is conformally situated on top of a curved gold surface. The curved gold surface causes serious bending of atomic bonds in MoS_2, leading to serious distortion of S-Mo-S lattice. The authors thus attributed the excellent HER performance (onset potential of -118 mV and Tafel slope of 46 mV dec^{-1}) to the tensile strain in the distorted MoS_2 lattice (Figure 14d). Suh *et al.* demonstrated enhanced HER activity by combination of tensile strain and phase transition caused by rolling up MoS_2 sheet (Figure 14e).[132] Transition from 2*H* to 1*T* phase in MoS_2 sheets was achieved by rolling up MoS_2 sheets to form scrolls due to intralayer plane gliding.[133] The authors further improved the gliding-rolling process by decorating the MoS_2 layer with Pt nanoparticles. As shown in Figure 14f, the rolled up MoS_2 decorated with Pt nanoparticle (MoS_2@Pt scroll) has both larger fraction of 1*T*-phase MoS_2 and higher strain up to 2.4%. Compared to MoS_2@Pt without gliding-rolling process, the MoS_2@Pt scroll further reduces the Tafel slope from 49 to 39 mV dec^{-1}. Nevertheless, the contribution of strain effect is not successfully decoupled from that of the phase transition effect.

4.2.3. Nanostructured Substrate Templated Strain

Motivated by these advances of strain engineering, we have developed a strain technique for monolayer 2D material that could (1) work on rigid substrate, and (2) create textured strain in a large area (details have been discussed in Figure 10).[57] We now discuss how this strain technique enhances the activity of a HER catalyst made of MoS_2 with sulfur vacancies (V-MoS_2).[65] As illustrated in **Figure 15**a, elastic tensile strain is applied to V-MoS_2 [rich of sulfur vacancies (S-vacancies)] that serve as the active sites. The tensile strain effectively moves both conduction bands and valence bands towards the Fermi level. This movement tunes the hydrogen adsorption free energy ΔG_H towards thermoneutral condition; and thus promotes the HER activity. Figure 15b compares the polarization curves of a few catalysts, *i.e.*, pristine MoS_2 (blue dashed curve), strained MoS_2 (S-MoS_2, the blue solid curve), V-MoS_2 (red dashed curve), strained V-MoS_2 (SV-MoS_2, the red solid curve), as well as Pt and Au substrate. The contributions of the tensile strain are highlighted by green color. The strain effect on pristine 2*H* MoS_2 is very limited because the reduced ΔG_H value of S-MoS_2 is still close to +2 eV, leading to very poor HER activity. In contrast, the strain effect on V-MoS_2 is very significant. As the ΔG_H value of V-MoS_2 is small, a further reduction of ΔG_H results in pronounced improvement in HER activity. Similar observations are found in decrease of Tafel slope, as presented in Figure 15c. The Tafel slope of S-MoS_2 is improved slightly in comparison to that of MoS_2 while the Tafel slope significantly decreases from 82 mV dec^{-1} (of V-MoS_2) to 60 mV dec^{-1} (of SV-MoS_2) for V-MoS_2. The much smaller Tafel slope suggests the much faster reaction kinetics, which will be detailed in later measurement. Figure 15d compares the intrinsic HER activity, TOF normalized to surface Mo atoms (TOF_{MO}). In order to emphasize the pure straining effect, the sole contribution of tensile strain is highlighted in green color in Figure 15b-d. One can see that indeed tensile strain significantly improves the TOF_{MO} of V-MoS_2, making it a much better HER catalyst.

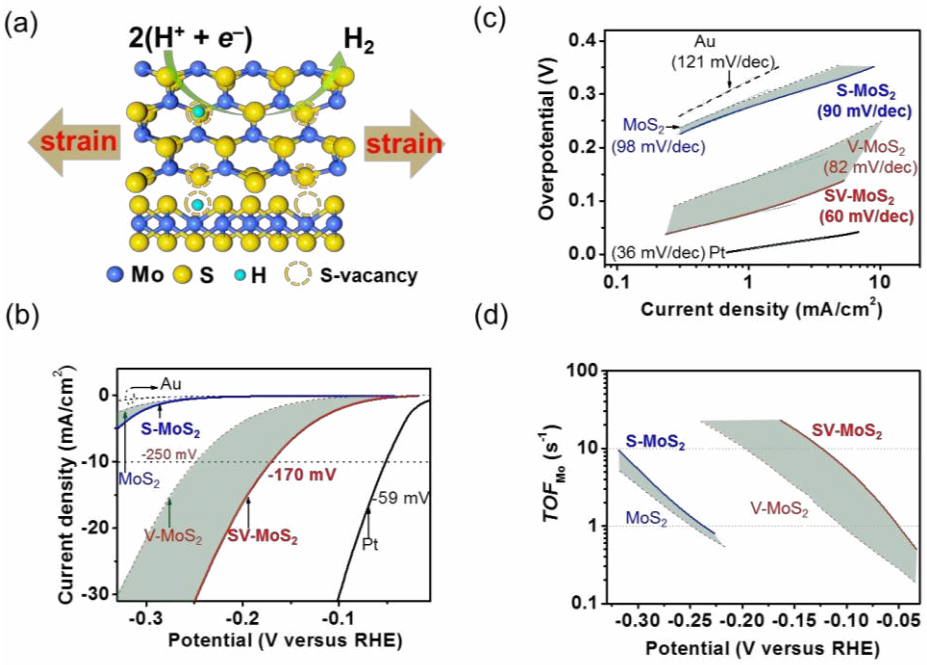

Figure 15. Nanostructured substrate induced textured strain for enhanced HER activity. (a) Schematic of strained MoS_2 with vacancy for HER. Upper panel: top view of a monolayer MoS_2. Low panel: side view of the monolayer MoS_2. The blue, yellow, cyan dots are the Mo, S and H atoms, respectively. The dashed circles are S-vacancy. (b) Polarization curves of gold substrate (Au), pristine MoS_2 (MoS_2), strained MoS_2 (S-MoS_2), MoS_2 with vacancy (V-MoS_2), strained V-MoS_2 (SV-MoS_2) and Pt electrode (from left to right). Overpotentials at 10 mA cm^{-2} are labelled. (c) Tafel plot of the materials in (b). (d) *TOF* normalized to surface Mo atoms (TOF_{MO}) of MoS_2, S-MoS_2, V-MoS_2 and SV-MoS_2 (from left to right). The green shaded areas in (b), (c) and (d) highlight the sole contribution of tensile strain. Reproduced with permission.[65] Copyright 2016 Springer Nature.

Lastly, we discuss about the first quantitative study of strain effect on the HER kinetics of 2D catalyst.[134] A scanning electrochemical microscopy (SECM) is employed to measure the HER kinetics, as illustrated in **Figure 16**a. SECM is essentially a typical three-electrode electrochemical cell coupled to a Pt ultramicroelectrode (UME). The Pt UME is used to oxidize the hydrogen molecules (via hydrogen oxidation reaction, *i.e.*, HOR: $1/2H^2 \rightarrow H^+ + e^-$) generated by HER on the catalyst surface, *i.e.*, S-MoS_2 or SV-MoS_2 in our case. The Pt UME is positioned close enough to the catalyst surface (within the H_2 diffusion layer of the catalyst), so that the HOR is controlled by the diffusion of H_2 molecules from the catalyst surface. In this case, the HOR and HER are linked together; and the unknown HER kinetics on MoS_2 catalyst could be obtained by fitting the measured curves with the well-known HOR

kinetics on Pt electrode as the input parameters. Figure 16b displays the simulated hydrogen concentration near the gap between Pt UME tip and SV-MoS_2 catalyst surface, where the Pt UME tip is well situated within the hydrogen diffusion layer. The Pt UME tip has a small diameter of 25 μm, avoiding its disturbance to HER below. The small area of HER working electrode (500 μm in diameter; see the optical image of a sample in Figure 16c) ensures the V-MoS_2 and SV-MoS_2 contain very similar MoS_2 flakes, minimizing the influence of the difference in materials. The distribution of strain in the strained MoS_2 by nanopillar array is depicted in Figure 16d, where textured tensile strain uniformly distributes across the sample is evident. A transient Pt UME tip current of V-MoS_2 is recorded when a pulse potential between the open circuit potential and -0.55 V vs. Ag/AgCl is applied to the V-MoS_2 substrate, as presented in Figure 16e, where the same response of SV-MoS_2 is also shown for comparison. One can see that tensile strain greatly increases the substrate current as highlighted by the green shaded areas. The pulse potential switches ON (at -0.55 V vs. Ag/AgCl) and OFF (at open circuit potential) the HER on MoS_2 working electrode, which should in turn switch ON and OFF the HOR on Pt UME tip if the HOR is controlled by the diffusion of H_2 molecules from HER. Indeed, the simultaneously recorded HOR current on Pt UME tip oscillates and synchronizes with the oscillating HER, as depicted in Figure 16e and 16f. These experiments have validated the proposed working principle of the measurement setup. By fitting the measurement results using a one-electron reaction model with a Butler-Volmer equation, we have found that the tensile strain boosted the HER kinetics of V-MoS_2 catalyst by more than 300%. This is the first quantitative study of the sole impact of strain on 2D HER catalyst.

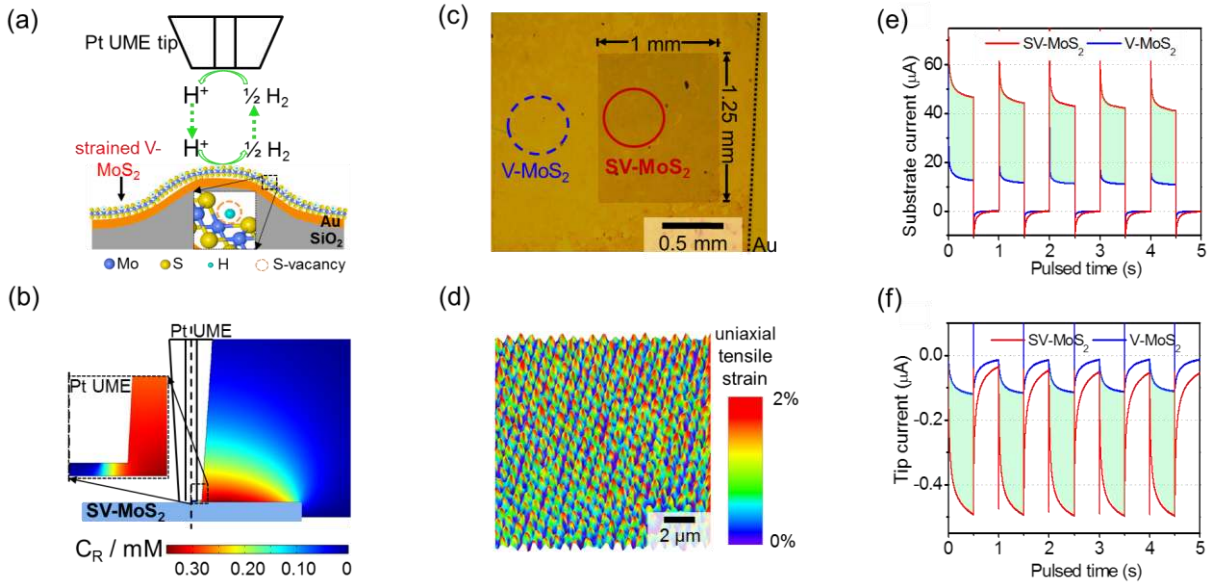

Figure 16. Quantitative investigation of strain-enhanced HER activity. (a) Schematic of the SECM measurement setup. The top trapezoid represents the Pt UME tip where HOR occurs, and the bottom strained V-MoS_2 on an Au nanopillar is the working electrode where HER occurs. (b) COMSOL simulated spatial distribution of hydrogen concentration (C_R/mM). The left inset shows the enlarged view of gap between Pt UME and SV-MoS_2. The lower inset is the color bar of hydrogen concentration. (c) An optical image of sample, where a nanopillar array with area of 1×1.25 mm^2 was patterned by electron beam lithography. The left and right circles label the place of V-MoS_2 and SV-MoS_2 working electrode, respectively. The area on the left of the black dotted line was covered by monolayer MoS_2 while that on the right was the bare Au surface. (d) The spatial distribution of tensile strain (calibrated to uniaxial) in a strain-textured MoS_2 monolayer on SiO_2/Si substrate. Inset: color bar of strain magnitude. The transient MoS_2 substrate current (e), and Pt UME tip current (f) of both V-MoS_2 and SV-MoS_2 working electrodes according to the double-pulse potential applied to the substrate. The tip potential was held at 0 V, and the substrate potential was switched between open circuit potential and -0.55 V vs. Ag/AgCl. The pulse width was 0.5 s with 5 replicates. The strain effect is highlighted by green shade areas in (e) and (f). Reproduced with permission.[134] Copyright 2016 American Chemical Society.

4.2.4. Proposed Techniques and Systems for Strain-Promoted Two-Dimensional Catalysts

Despite the significant positive impact of strain engineering in electrochemistry, particularly the reaction involving 2D catalysts, there is little development in this area due to the lack of appropriate straining technique for electrochemical reactions. Herein, we propose a few strategies to implement strain engineering in electrochemical reactions, as illustrated in **Figure 17**. The first proposal is to introduce strain by bending or elongating a flexible holder where the 2D catalyst is attached (similar to those in Figure 9), as shown in Figure 17a. The lower end of the flexible holder (*e.g.*, PET film) is fixed to the bottom of the reaction cell

while the upper end is fixed to a movable part outside of the reaction cell. The movable part could be moved up or down by turning the screws attached. The length of the flexible holder is adjusted so that proper amount of strain could be created by tuning the screw in its full range of track. 2D catalyst is transferred to the flexible holder and could be fixed by glue or clamp on its perimeter. Alternatively, Nafion membrane can be employed to passivate the catalyst (*e.g.*, by hot press). Conductive wire connecting between the catalyst and the working electrode (WE) is covered by insulating glue. This setup allows quick test of strained 2D catalyst in a few % of both compressive and tensile strains depending on bending forward or backward, as discussed in Figure 9e.

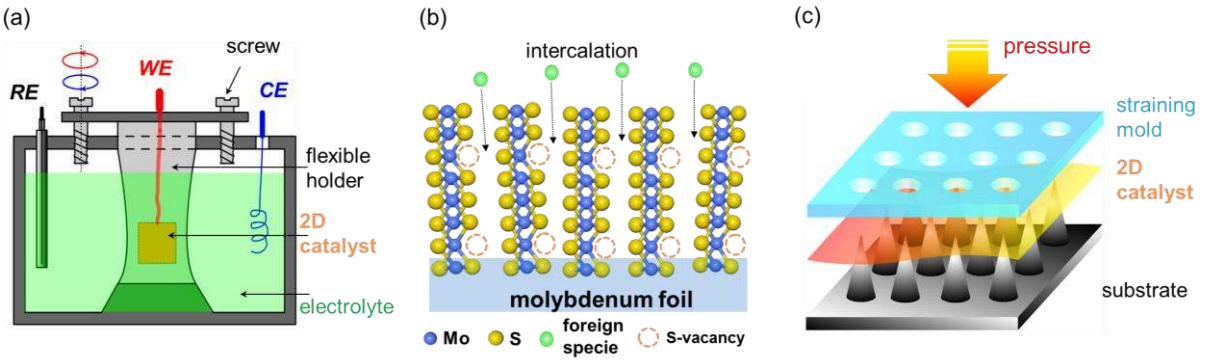

Figure 17. Proposed straining methods and systems for 2D electrochemical catalysts. (a) Bending substrate incorporated in reaction cell. The screws are used to control the bending (clockwise turning) or elongation (counterclockwise turning) of the flexible holder where the 2D catalyst is attached. RE, WE and CE represent reference electrode, working electrode and counter electrode, respectively. (b) Controlled ion intercalation for tunable strain in vertical 2D catalyst. MoS_2 with sulfur vacancies is taken as an example, which could be directly grown in sulfur deficient environment on molybdenum metal foil. The blue, yellow and green dots represent the Mo atom, S atom and intercalated foreign species, respectively. The dotted circle delineates S-vacancy. (c) Template-induced texture strain (nanoindentation like) in 2D catalyst. The 2D catalyst is sandwiched between a nanostructured substrate and its complementary straining mold. Upon pressure on the straining mold, textured tensile strain will be created in 2D catalyst; and the strain magnitude depends on the pressure.

The second proposal utilizes the ion intercalation process to control the strain in vertically aligned 2D catalyst, as illustrated in Figure 17b. For instance, MoS_2 film could be grown vertically from thick Mo film due to the much smaller strain energy compared to that horizontal growth; because significant volume expansion occurs during sulfurization of Mo to

form MoS_2.[135],[136] Fast sulfurization or nonstoichiometric growth process thus could embed compressive strain and sulfur vacancies in vertical MoS_2 film.[137] Intercalation of foreign species into the MoS_2 film can tune the strain by expanding the interlayer distance up to 1.45 nm.[138-140] The increased interlayer distance with modified electronic structure is beneficial for HER activities.[141] Phase changing could also occur during intercalation as well, particularly lithium ion intercalation, which introduces lattice-mismatch-induced strain, and thus tune the catalytic activity.[142] This proposed structure has a few advantages as a catalyst. Firstly, the vertical structure ensures each individual MoS_2 layer is in contact with the conductive substrate Mo foil. Secondly, the direct growth process offers the optimal contact interface between MoS_2 and substrate. Thirdly, the strain inside the film is tunable by choosing different intercalation species or by varying the intercalation process parameters. Fourthly, the tunable height of the MoS_2 layer makes it easy to balance the tradeoff between performance and lifetime (thicker MoS_2 has longer lifetime while probably poorer performance). Thus, this proposed structure could serve as a generic design for strained 2D catalysts.

The third proposal makes use of the template-induced texture strain, as shown in Figure 17c. A 2D catalyst film is transferred onto a nanostructured substrate such as a nanoneedle array that has a complementary mesh-like mold. When the strain mold is pressed against the nanoneedle array, the 2D catalyst sandwiched in the middle will be strained. The strained part of 2D catalyst will be exposed to the electrolyte via the holes of the mold. The strain profile can be changed by varying the structure of the substrate and its associated complementary mold. The magnitude of the strain can be tuned by the pressure applied on the straining mold. The advantages of this method include (1) extreme strain (up to the breaking strength of the 2D catalyst) could be applied, (2) 2D catalyst with a range of thicknesses (from monolayer to thick film) could be strained, and (3) the strain profile and distribution could be easily varied. Thus, this proposal could offer a solution to study 2D catalyst under large strain and

especially patterned strain along certain lattice directions.

5. Strain-Promoted Oxygen Evolution Reaction

At present, OER is still the bottleneck of overall water splitting and demands a much higher overpotential to match the reaction rate of HER due to its relatively more sluggish kinetics. Transition-metal-based oxides, hydroxides, and (oxy)hydroxide exhibit attractive OER activities. Graphene-like 2D materials, particularly TMDs, have very limited application for OER due to their instability in oxidative environment; we thus only discuss oxides as OER catalysts. Improving OER activities of oxide needs various nanotechnologies. Specifically, elastic strain is being increasingly employed to enhance the catalytic properties of mixed metal oxides.[143] Through first-principles calculations, Yildiz *et al*. demonstrated that oxygen adsorption on $LaCoO_3$ are facilitated by elastic stretching and a transition from chemisorption to physisorption of the oxygen molecule is identified at high strains. Combing with charge-density profiles, density of electronic states, and stress thresholds, they suggested the possibility of tuning strain-mediated reactivity in $LaCoO_3$ and related perovskite oxides.[144] Following that, numerous studies have investigated the effect of strain on the surface reactivity. The best available catalyst compromising superior OER activity and stability at the acidic solution is presently iridium oxide, while it is prohibitively expensive for large-scale applications because of the high cost of iridium. Koper's group reported a class of OER electrocatalysts based on iridium double perovskites that contain 32 wt% less iridium and yet exhibit a more than threefold higher activity than IrO_2 in acid media, along with robust durability.[145] Double perovskites (DPs) are compounds with the generic formula $A_2BB'O_6$, with A denoting a large cation, and B and B' smaller cations, as shown in **Figure 18**a. Regarding the high activity measured for the Ir DPs, they postulated that the crystal lattice strain caused by the small lanthanide and yttrium cations in the B' site of the DPs could be related to the enhanced OER activity for the corresponding compounds (Figure 18b). DFT

calculations have shown that the substitution for smaller A-site cations can decrease oxygen adsorption energies on simple perovskites (ABO_3), due to the crystal strain. Owing to the strong binding of IrO_2 with oxygen, the lattice strain caused by substitution of smaller lanthanides or yttrium could weaken the oxygen adsorption energy and therefore improve the activity of the Ir DPs in comparison with IrO_2. The effect of strain in the crystal lattice on OER activity of the Ir DPs was further confirmed by comparing the activity measured for Ba_2YIrO_6 and Sr_2YIrO_6. Besides, the authors also evaluated the electrochemical stability of the Ir DPs in acid medium by galvanostatic electrolysis at 10 mA cm^{-2} (Figure 18 c and 18d). The stability of IrO_2 nanoparticles was tested for comparison as well. Figure 18 c shows that Ba_2PrIrO_6 and Ba_2YIrO_6 DPs are electrochemically stable on the time scale of 1 h, similar to IrO_2 nanoparticles. In fact, the chronopotentiometry experiments at 10 mA cm^{-2} display better stability for both Ba_2PrIrO_6 and Ba_2YIrO_6 DPs in comparison with that of IrO_2 catalyst (Figure 18d). Although the La, Nd and Tb-containing DPs are also very active, they lose their activity after 1-h galvanostatic electrolysis (Figure 18c).

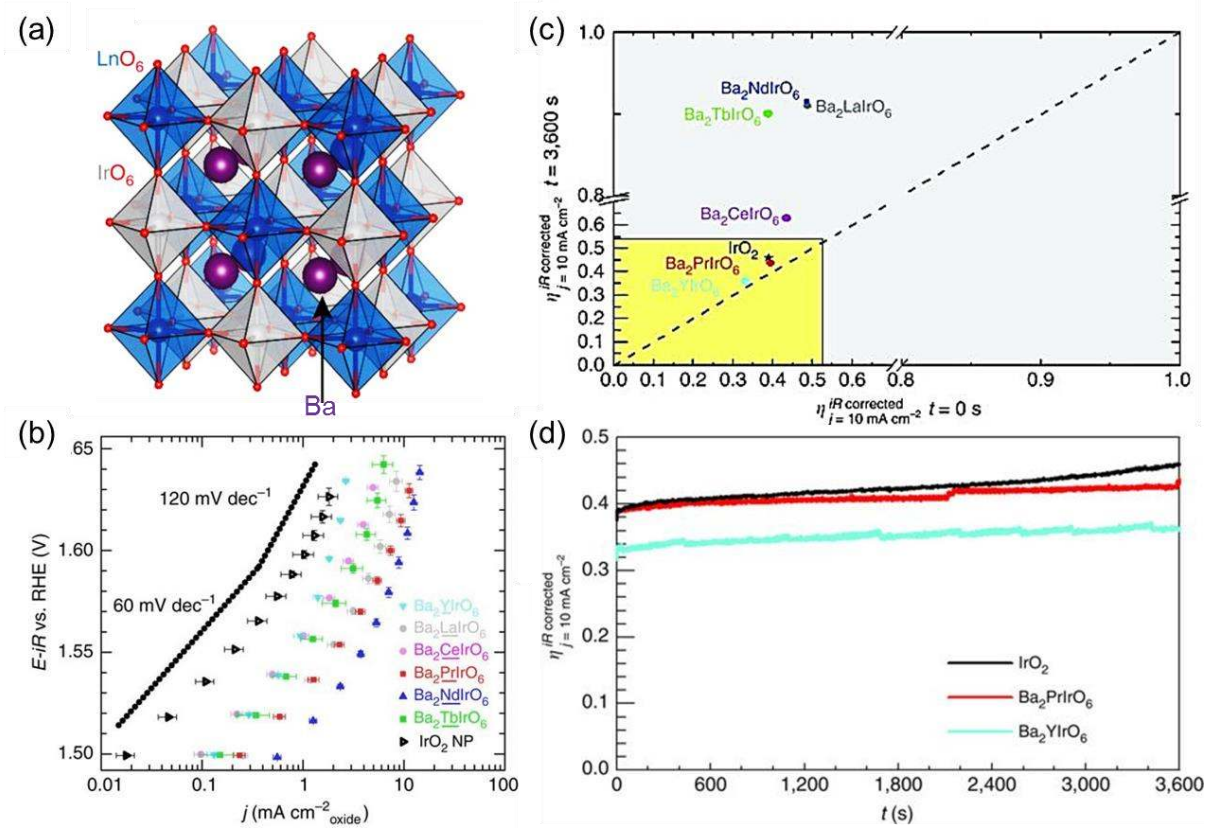

Figure 18. Effect of lattice strain on OER activities of iridium double perovskite. (a) Crystal structure of a generic Ba_2MIrO_6 DP. (b) OER activity in 0.1M $HClO_4$ of Ba_2MIrO_6, M=Y, La, Ce, Pr, Nd, Tb, compared with the benchmark activity of IrO_2 nanoparticles. (c) OER overpotential measured on the Ir DPs after 1 h of galvanostatic electrolysis plotted as a function of the initial overpotential. (b) Evolution of the OER overpotential on $Ba_2PrIrO6$, Ba_2YIrO_6 DPs and IrO_2 nanoparticles during 1 h of galvanostatic electrolysis. Reproduced with permission.[145] Copyright 2016, Springer Nature.

In addition, the catalytic impact of strain on transition-metal oxide thin films except for noble-metal oxide has also been reported. Lee's group epitaxially strained the conducting perovskite $LaNiO_3$ (LNO) ranging from tensile (+) to compressive (−) to systematically determine its influence on OER by using pulsed laser epitaxy on a range of lattice-mismatched substrates including (001) $LaSrAlO_4$ (LSAO), (001) $LaAlO_3$ (LAO), (001) $(LaAlO3)_{0.3}(SrAl_{0.5}Ta_{0.5}O_3)_{0.7}$ (LSAT), (001) $SrTiO_3$ (STO), and $(001)_{pc}$ $DyScO_3$ (DSO).[46] These resulting 10 nm thick (001)-oriented films are under biaxial strain from 2.7 to -1.2% (**Figure 19**a). Uniquely, they found that compressive rather than tensile strain could significantly enhance the OER reaction in 0.1M KOH solution (Figure 19b). To get more in-depth examination of the relationship between OER activity and strain, the authors performed a series of physiochemical characterizations (Figure 19c-e). Synchrotron X-ray linear dichroism (XLD) was first employed to resolve the orbital splitting energies and e_g^1 occupancies between the d_z^2 and $d_{x^2-y^2}$ orbitals. By detecting the absorption of X-rays polarized both perpendicular (E // c) and parallel to the film plane (E // ab), the respective energies and unoccupied states (holes) of the d_z^2 and $d_{x^2-y^2}$ orbitals can be probed. It was found that compressive strain reduces the peak energy of the d_z^2 orbital relative to the $d_{x^2-y^2}$ orbital by comparing the difference in the peak energy values between the *c*- and *ab*-axes edges. Obviously, tensile strain had the opposite effect. By plotting this peak position and orbital occupancy versus strain in Figure 19c, they found that compressive strain-induced orbital splitting results in a lower-energy, high-occupancy d_z^2 ($d_{x^2-y^2}$) orbital. Then, this orbital splitting was also determined by calculating the centroid of all states for each orbital

relative to E_F (analogous to the *d*-band center in metals) on the basis of DFT, and the orbital polarization was found by calculating the orbital e^- occupancy. As seen in Figure 19d, DFT calculations for the bulk matched well with the experimental XLD results, where compressive strain favored a more polarized and lower energy d_{z^2} ($d_{x^2-y^2}$) orbital. However, the surface calculations disclosed much difference due to the asymmetry resulting from the lack of an apical oxygen atom on the surface NiO_6 octahedra. This asymmetry lead to a ~ 1 eV decrease (increase) in the center of the d_{z^2} ($d_{x^2-y^2}$) orbital relative to E_F. Even though strain-induced orbital splitting still occurred at the surface, these offsets resulted in the d_{z^2} ($d_{x^2-y^2}$) orbital center lying below (above) E_F over the entire strain range. Correspondingly, as shown in Figure 19e, the orbital polarization at the surface was shifted toward the d_{z^2} orbital. Indeed, the occupancy of this orbital in unstrained LNO increased from ~ 55% of e_g^1 in the bulk to ~ 80% at the surface. Thus, the asymmetry at the surface dramatically favored occupancy of the d_{z^2} orbital over the $d_{x^2-y^2}$ orbital. Similar to strain-induced shifts in the *d*-band center of noble metals relative to the Fermi level; such splitting can dramatically affect OER activity in this perovskite by tuning the M-O chemisorption.

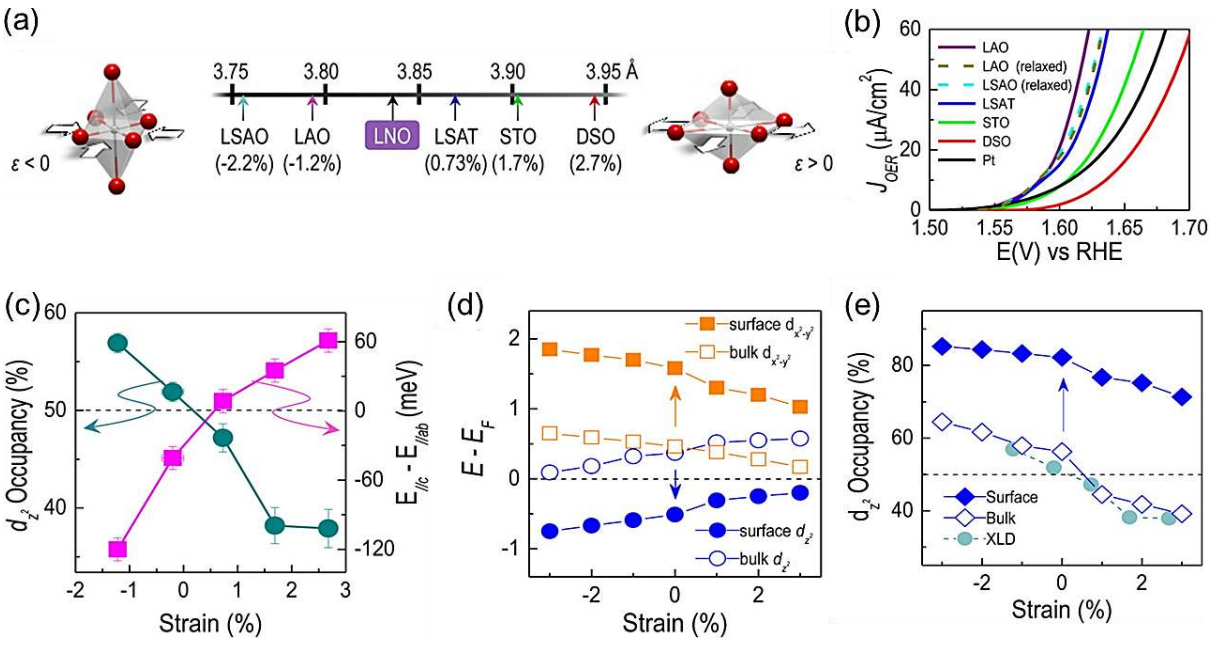

Figure 19. Effects of lattice-mismatch induced strain on OER performance of $LaNiO_3$. (a) Lattice parameters and associated biaxial strain for $LaNiO_3$ (LNO) on various substrates. (b) OER on these strained LNO films. Strain-relaxed ($\varepsilon \sim 0\%$) films grown on $LaSrAlO_4$ (10 nm in film thickness) and on $LaAlO_3$ (100 nm in film thickness) as well as Pt films for comparison. (c) The plots of strain-induced changes in the occupancy of the d_z^2 orbital along with the relative energy positions of the d_z^2 orbital compared to the $d_{x^2-y^2}$ orbital (E_c-E_{ab}) by using sum rules. (d) Strain-dependent changes in the centroid position of density of states (DOS) for the d_z^2 and $d_{x^2-y^2}$ orbitals with respect to E_F for both the LNO bulk and surface. Arrows are used to guide the eye from bulk to surface data. (e) Modeled orbital polarization in the bulk and the surface. Reproduced with permission.[46] Copyright 2016 American Chemical Society.

Interestingly, the same group subsequently found that epitaxial tensile strain is a powerful tool for manipulating the oxygen content of perovskite-based strontium cobaltite ($SrCoO_x$), yielding increasingly oxygen-deficient states. The additional oxygen vacancies enhanced the cobaltite's catalytic activity toward OER by over an order of magnitude, equaling that of precious-metal catalysts, including IrO_2.[146] They used this control over the oxygen content to artificially tune the oxygen vacancies in the oxidized perovskite phase of $SrCoO_x$ (P-SCO) and thus optimizing OER activity. To inspect topotactic oxidation to P-SCO under OER conditions, a series of pre-oxidized brownmillerite phase $SrCoO_{2.5}$ (BM-SCO) films were epitaxially grown on lattice-mismatched substrates using the similar pulsed laser epitaxy. The uniform and thin thickness of 15 nm minimized strain relaxation on substrates, leading to substrate-induced tensile strains (ε) from 1.0 to 4.2% for fully oxidized SCO. **Figure 20**a shows the plot of the P-SCO c parameter versus strain compared to results from previous bulk (unstrained) P-SCO studies. For the nearly fully stoichiometric P-SCO, there was a clear linear shift in the c parameter that can be attributed to a Poisson-type contraction with a ratio of about 0.26. In contrast, for the coherently deposited, electrochemically oxidized films, the monotonic shift in the c parameter increasingly diverged from this stoichiometric behavior with tensile strain $\varepsilon > 1\%$ because of the increase in the degree of oxygen deficiencies throughout the film. Direct-current electrical transport measurements at room temperature (Figure 20b) further supported this systematic change in stoichiometry for $\varepsilon > 1\%$. As the

tensile strain increased, the film became less conducting, suggesting a higher concentration of oxygen vacancies and the lower ratio of fully oxidized Co^{4+} and lower-energy Co^{3+} (Figure 20c). It is expected that all the above changes gave rise to different OER activities (Figure 20d and 20e). Figure 20d exhibits polarization curves of OER for strained P-SCO. As the tensile strain in P-SCO increased from 0 to 4.2%, the onset potential for the OER was reduced by ~100 mV towards that of IrO_2. The inverse relationship between catalytic activity and conductivity (Figure 20b) suggested that charge transfer considerations do not hinder the OER reaction. Similarly, Shao-Horn *et al*. demonstrated that epitaxial strain can tune the activity of oxygen electrocatalysis in alkaline solutions for $LaCoO_3$, where moderate tensile strain can further induce changes in the electronic structure; leading to increased activity.[147] Thus, a balance between tensile strain and electronic conductivity must be achieved to maximize catalytic activity.

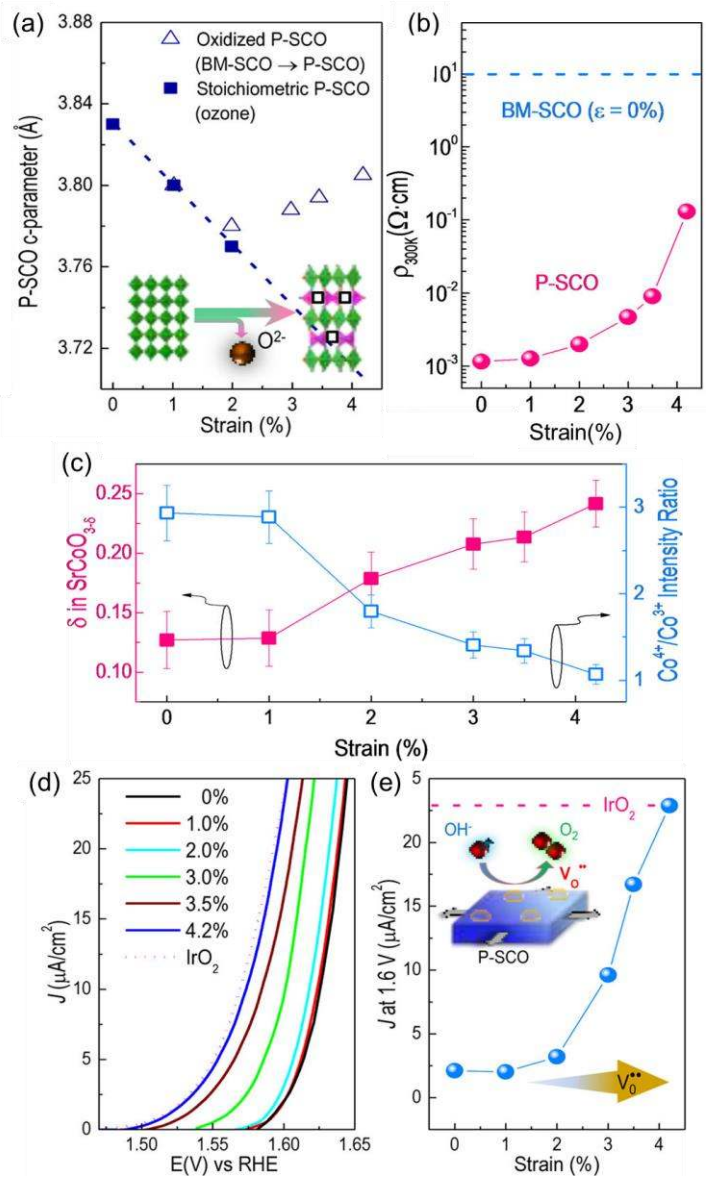

Figure 20. Effects of epitaxial growth-induce strain on OER performance of P-SCO. (a) Deviation of the out-of-plane *c* parameter from the stoichiometric Poisson ratio of ~0.26 is due to oxygen vacancy formation. (b) Increase in the resistivity of strained P-SCO films at room temperature due to strain-induced loss of oxygen. (c) Plot of the ratio of the intensities of the Co^{4+}/Co^{3+} peaks showing a clear trend toward decreasing Co valence with tensile strain, with a matching trend in oxygen nonstoichiometry (δ). (d) Polarization curves for the OER reaction on P-SCO under increasing amounts of biaxial tensile strain. (e) Current densities at 1.6 V vs. RHE for all of the films are plotted as a function of strain. The activity for a textured (111) IrO_2 film is included. Reproduced with permission.[146] Copyright 2016 American Chemical Society.

Since most of 2D chalcogenides are not stable at OER condition, strain-promoted 2D chalcogenides for catalyzing OER has not been reported yet. However, there are a few report of strained layer double hydroxide[148] or platelet perovskite catalyst.[46, 149] With the

continuous development of various metal oxide OER catalysts,[150-153] we believe strain effect will be soon explored in these 2D OER catalysts.

6. Conclusions and Outlook

This review has profiled ongoing research efforts on the strain engineering of a variety of electrocatalysts, which include noble metals, 2D transition-metals-based nanomaterials, and perovskite oxides for both hydrogen and oxygen reactions (HER and OER) in water electrolysis. Density functional theory (DFT) continues to serve as a framework to understand the scaling limitations across a range of existing electrocatalytic systems for HER and OER at the atomistic surface level, and from it, guide the use of strain to tune the adsorption properties of existing materials and then to optimize catalytic performance. A range of strategies for tuning strain on electrocatalytic systems have been summarized, which include crystal shaping, porosity controlling, alloying, doping, epitaxial growth and solid mechanic approaches. Despite these advances, several challenges still remain:

(1) *Decoupling strain effect*. The strain is usually co-created with other factors such as vacancy and defect, which complicate the identification of the strain-activity correlation. It still needs well-defined model systems and precise strain generation strategy for decoupling the multiple effects of strain. Such complex synergistic effects arising from strain and other factors necessitate complementary experimental and theoretical studies for comprehensive understanding of the catalytic process. Those synergistic effects also offer new opportunities to optimize electrocatalytic properties.

(2) *In-situ characterizations*. At present, there are a large number of physiochemical characterizations for bulk strain, such as aberration-corrected high-resolution scanning transmission electron microscopy, coherent X-ray diffractive imaging, X-ray reciprocal space mapping, Raman spectroscopy, band-excitation switching spectroscopy, photoluminescence spectroscopy, high-resolution soft X-ray absorption spectroscopy (XAS), bulk-sensitive hard

X-ray photoemission spectroscopy (HAXPES) mapping, and 3D Bragg projection ptychography. However, electrochemical reactions occur at the surface of catalysts, so these bulk strain measurements may not reflect the true relation of strain-catalytic activities of catalysts. Scanning electrochemical microscopy (SECM) may be a suitable candidate for in-situ studies of the impact of strain on catalytic activities. However, the resolution of SECM is not high enough for current researches. It's still highly urgent to develop novel and effective characterization techniques for in-situ monitoring of catalytic reactions.

(3) *Extending strain applications*. Many efforts have been devoted to noble metals or their alloys with different nanoarchitectures, two-dimensional TMDs such as MoS_2, WS_2, *etc*., and perovskite oxides, while little attention has been paid on other extremely promising water splitting catalysts, such as transition-metal carbides, phosphides, and selenides for HER; transition-metal oxides/hydroxides/(oxy)hydroxides for OER.

(4) *Outlook on DFT modelling of HER and OER.* While DFT has provided insights for HER kinetics of metallic systems with well-determined active sites, it still has difficulty determining a clear mechanistic pathway for systems, which have multifunctional active sites (*e.g*., metal sulfides and metal phosphides, doped or undoped). In OER systems, similar challenges exist for novel materials. The role of water at the interface also continues to be an active area of research. Although the use of d-band theory and DFT have been sufficient in describing and rationalizing the use of lattice strain to optimize adsorption of certain intermediates, the direct translation of simulated systems with elastic strain to experimental work remains an challenge. This is usually due to stability issues of the actual system under lattice strain. Therefore, DFT may also be used to explore routes to properly synthesize stable surfaces and control uniform lattice strain on catalytic material systems. DFT can also be used to diagnose the severity of other factors, such as geometric size effects, competing against lattice strain effects. Doing so would enable ways to decouple these effects from lattice strain effects. Importantly, DFT modeling could provide unique insight into the synergistic effects

between strain and other factors, which are unlikely to be observed or quantified experimentally, in the electrode with complicated structure and composition.

Acknowledgements
This work was supported by Nanyang Technological University under NAP award (M408050000) and Tier 1 RG101/18 (2018-T1-001-051).

Received: ((will be filled in by the editorial staff))
Revised: ((will be filled in by the editorial staff))
Published online: ((will be filled in by the editorial staff))

References

[1] S. Chu, Y. Cui, N. Liu, *Nat. Mater.* **2016**, 16, 16-22.

[2] Y. Jiao, Y. Zheng, M. Jaroniec, S. Z. Qiao, *Chem. Soc. Rev.* **2015**, 44, 2060-2086.

[3] B. You, Y. Sun, *Acc. Chem. Res.* **2018**, 51, 1571-1580.

[4] B. M. Hunter, H. B. Gray, A. M. Muller, *Chem. Rev.* **2016**, 116, 14120-14136.

[5] N. T. Suen, S. F. Hung, Q. Quan, N. Zhang, Y. J. Xu, H. M. Chen, *Chem. Soc. Rev.* **2017**, 46, 337-365.

[6] B. You, G. Han, Y. Sun, *Chem. Commun.* **2018**, 54, 5943-5955.

[7] C. G. Morales-Guio, X. Hu, *Acc. Chem. Res.* **2014**, 47, 2671-2681.

[8] D. Kang, T. W. Kim, S. R. Kubota, A. C. Cardiel, H. G. Cha, K. S. Choi, *Chem. Rev.* **2015**, 115, 12839-12887.

[9] V. R. Stamenkovic, D. Strmcnik, P. P. Lopes, N. M. Markovic, *Nat. Mater.* **2016**, 16, 57-69.

[10] D. G. Nocera, *Acc. Chem. Res.* **2017**, 50, 616-619.

[11] Y. Zheng, Y. Jiao, M. Jaroniec, S. Z. Qiao, *Angew. Chem. Int. Ed.* **2015**, 54, 52-65.

[12] Y. Liang, Y. Li, H. Wang, H. Dai, *J. Am. Chem. Soc.* **2013**, 135, 2013-2036.

[13] B. You, Y. Sun, *ChemPlusChem* **2016**, 81, 1045-1055.

[14] I. Roger, M. A. Shipman, M. D. Symes, *Nat. Rev. Chem.* **2017**, 1, 0003.

[15] Q. Ding, B. Song, P. Xu, S. Jin, *Chem* **2016**, 1, 699-726.

[16] B. You, N. Jiang, M. Sheng, M. W. Bhushan, Y. Sun, *ACS Catal.* **2015**, 6, 714-721.

[17] N. Jiang, B. You, M. Sheng, Y. Sun, *Angew. Chem. Int. Ed.* **2015**, 54, 6251-6254.

[18] B. You, N. Jiang, M. Sheng, S. Gul, J. Yano, Y. Sun, *Chem. Mater.* **2015**, 27, 7636-7642.

[19] B. You, Y. Sun, *Adv. Energy Mater.* **2016**, 6, 1502333.

[20] H. Wang, H. W. Lee, Y. Deng, Z. Lu, P. C. Hsu, Y. Liu, D. Lin, Y. Cui, *Nat. Commun.* **2015**, 6, 7261.

[21] S. Anantharaj, S. R. Ede, K. Sakthikumar, K. Karthick, S. Mishra, S. Kundu, *ACS Catal.* **2016**, 8069-8097.

[22] B. You, X. Liu, G. Hu, S. Gul, J. Yano, D. E. Jiang, Y. Sun, *J. Am. Chem. Soc.* **2017**, 139, 12283-12290.

[23] R. Subbaraman, D. Tripkovic, D. Strmcnik, K. C. Chang, M. Uchimura, A. P. Paulikas, V. Stamenkovic, N. M. Markovic, *Science* **2011**, 334, 1256-1260.

[24] R. Subbaraman, D. Tripkovic, K. C. Chang, D. Strmcnik, A. P. Paulikas, P. Hirunsit, M. Chan, J. Greeley, V. Stamenkovic, N. M. Markovic, *Nat. Mater.* **2012**, 11, 550-557.

[25] I. Ledezma-Yanez, W. D. Z. Wallace, P. Sebastián-Pascual, V. Climent, J. M. Feliu, M. T. M. Koper, *Nat. Energy* **2017**, 2, 17031.

[26] C. Chen, Y. Kang, Z. Huo, Z. Zhu, W. Huang, H. L. Xin, J. D. Snyder, D. Li, J. A. Herron, M. Mavrikakis, M. Chi, K. L. More, Y. Li, N. M. Markovic, G. A. Somorjai, P. Yang, V. R. Stamenkovic, *Science* **2014**, 343, 1339-1343.

[27] C. Niether, S. Faure, A. Bordet, J. Deseure, M. Chatenet, J. Carrey, B. Chaudret, A. Rouet, *Nat. Energy* **2018**, 3, 476-483.

[28] G. Liu, P. Li, G. Zhao, X. Wang, J. Kong, H. Liu, H. Zhang, K. Chang, X. Meng, T. Kako, J. Ye, *J. Am. Chem. Soc.* **2016**, 138, 9128-9136.

[29] Y. Shi, J. Wang, C. Wang, T.-T. Zhai, W.-J. Bao, J.-J. Xu, X.-H. Xia, H.-Y. Chen, *J. Am. Chem. Soc.* **2015**, 137, 7365-7370.

[30] M. Luo, S. Guo, *Nat. Rev. Mater.* **2017**, 2, 17059.

[31] B. T. Sneed, A. P. Young, C. K. Tsung, *Nanoscale* **2015**, 7, 12248-12265.

[32] C. Becher, L. Maurel, U. Aschauer, M. Lilienblum, C. Magén, D. Meier, E. Langenberg, M. Trassin, J. Blasco, I. P. Krug, P. A. Algarabel, N. A. Spaldin, J. A. Pardo, M. Fiebig, *Nat. Nanotech.* **2015**, 10, 661-665.

[33] P. R. Chidambaram, C. Bowen, S. Chakravarthi, C. Machala, R. Wise, *IEEE Trans. Electron. Devices* **2006**, 53, 944-964.

[34] S.W. Bedell, A. Khakifirooz, D. K. Sadana, *MRS Bull.* **2013**, 39, 131-137.

[35] J. Li, Z. Shan, E. Ma, *MRS Bull.* **2013**, 39, 108-114.

[36] B. Yildiz, *MRS Bull.* **2014**, 39, 147-156.

[37] Z. Huang, R. Boulatov, *Chem. Soc. Rev.* **2011**, 40, 2359-2384.

[38] G. Apai, J. F. Hamilton, J. Stohr, A. Thompson, *Phys. Rev. Lett.* **1979**, 43, 165-169.

[39] J. K. Nørskov, F. Abild-Pedersen, F, Studta, T. Bligaardc, *Proc. Natl. Acad. Sci. USA* **2011**, 108, 937-943.

[40] B. T. Sneed, C. N. Brodsky, C.-H. Kuo, L. K. Lamontagne, Y. Jiang, Y. Wang, F. Tao, W. Huang, C.-K. Tsung, *J. Am. Chem. Soc.* **2013**, 135, 14691-14700.

[41] P. Strasser, S. Koh, T. Anniyev, J. Greeley, K. More, C. Yu, Z. Liu, S. Kaya, D. Nordlund, H. Ogasawara, M. F. Toney, A. Nilsson, *Nat. Chem.* **2010**, 2, 454-460.

[42] T. A. Maark, A. A. Peterson, *J. Phys. Chem. C* **2014**, 118, 4275-4281.

[43] H. A. Tahini, X. Tan, U. Schwingenschlögl, S. C. Smith, *ACS Catal.* **2016**, 6, 5565-5570.

[44] Z. Lu, G. Chen, Y. Li, H. Wang, J. Xie, L. Liao, C. Liu, Y. Liu, T. Wu, Y. Li, A. C. Luntz, M. Bajdich, Y. Cui, *J. Am. Chem. Soc.* **2017**, 139, 6270-6276.

[45] E. L. Clark, C. Hahn, T. F. Jaramillo, A. T. Bell, *J. Am. Chem. Soc.* **2017**, 139, 15848-15857.

[46] J. R. Petrie, V. R. Cooper, J. W. Freeland, T. L. Meyer, Z. Zhang, D. A. Lutterman, H. N. Lee, *J. Am. Chem. Soc.* **2016**, 138, 2488-2491.

[47] C. Tsai, K. Chan, J. K. Nørskov, F. Abild-Pedersen, *J. Phys. Chem. Lett.* **2014**, 5, 3884-3889.

[48] J. Greeley, T. F. Jaramillo, J. Bonde, I. B. Chorkendorff, J. K. Nørskov, *Nat. Mater.* **2006**, 5, 909-913.

[49] Y. Jiao, Y. Zheng, K. Davey, S. Z. Qiao, *Nat. Energy* **2016**, 1, 16130.

[50] Z. W. Seh, J. Kibsgaard, C. F. Dickens, I. Chorkendorff, J. K. Nørskov, T. F. Jaramillo, *Science* **2017**, 355, eaad4998.

[51] X. Shi, S. Siahrostami, G.-L. Li, Y. Zhang, P. Chakthranont, F. Studt, T. F. Jaramillo, X. Zheng, J. K. Nørskov, *Nat. Commun.* **2017**, 8, 701.

[52] Y. Jiao, Y. Zheng, P. Chen, M. Jaroniec, S. Z. Qiao, *J. Am. Chem. Soc.* **2017**, 139, 18093-18100.

[53] H.-J. Chun, V. Apaja, A. Clayborne, K. Honkala, J. Greeley, *ACS Catal.* **2017**, 7, 3869-3882.

[54] J. Zhao, Z. Chen, *J. Am. Chem. Soc.* **2017**, 139, 12480-12487.

[55] Y. Abghoui, A. L. Garden, J. G. Howalt, T. Vegge, E. Skúlason, *ACS Catal.* **2015**, 635-646.

[56] G. Jones, T. Bligaard, F. Abild-Pedersen, J. K. Nørskov, *J. Phys. Condens. Matter.* **2008**, 20, 064239.

[57] H. Li, A. W. Contryman, X. Qian, S. M. Ardakani, Y. Gong, X. Wang, J. M. Weisse, C. H. Lee, J. Zhao, P. M. Ajayan, J. Li, H. C. Manoharan, X. Zheng, *Nat. Commun.* **2015**, 6, 7381.

[58] J. K. Nørskov, T. Bligaard, J. Rossmeisl, C. H. Christensen, *Nat. Chem.* **2009**, 1, 37-46.

[59] A. B. Laursen, A. S. Varela, F. Dionigi, H. Fanchiu, C. Miller, O. L. Trinhammer, J. Rossmeisl, S. Dahl, *J. Chem. Educ.* **2012**, 89, 1595-1599.

[60] A. Hellman, E. J. Baerends, M. Biczysko, T. Bligaard, C. H. Christensen, D. C. Clary, S. Dahl, R. van Harrevelt, K. Honkala, H. Jonsson, G. J. Kroes, M. Luppi, U. Manthe, J. K.

Nørskov, R. A. Olsen, J. Rossmeisl, E. Skúlason, C. S. Tautermann, A. J. C. Varandas, J. K. Vincent, *J. Phys. Chem. B* **2006**, 110, 17719-17735.

[61] E. Skúlason, V. Tripkovic, M. E. Björketun, S. Gudmundsdóttir, G. Karlberg, J. Rossmeisl, T. Bligaard, H. Jónsson, J. K. Nørskov, *J. Phys. Chem. C* **2010**, 114, 18182-18197.

[62] I. C. Man, H.-Y. Su, F. Calle-Vallejo, H. A. Hansen, J. I. Martínez, N. G. Inoglu, J. Kitchin, T. F. Jaramillo, J. K. Nørskov, J. Rossmeisl, *ChemCatChem* **2011**, 3, 1159-1165.

[63] L. C. Seitz, C. F. Dickens, K. Nishio, Y. Hikita, J. Montoya, A. Doyle, C. Kirk, A. Vojvodic, H. Y. Hwang, J. K. Nørskov, T. F. Jaramillo, *Science* **2016**, 353, 1011-1014.

[64] B. Hinnemann, P. G. Moses, J. Bonde, K. P. Jørgensen, J. H. Nielsen, S. Horch, I. Chorkendorff, J. K. Nørskov, *J. Am. Chem. Soc.* **2005**, 127, 5308-5309.

[65] H. Li, C. Tsai, A. L. Koh, L. Cai, A. W. Contryman, A. H. Fragapane, J. Zhao, H. S. Han, H. C. Manoharan, F. Abild-Pedersen, J. K. Nørskov, X. Zheng, *Nat. Mater.* **2016**, 15, 48-53.

[66] C. Tsai, H. Li, S. Park, J. Park, H. S. Han, J. K. Nørskov, X. Zheng, F. Abild-Pedersen, *Nat. Commun.* **2017**, 8, 15113.

[67] A. Leonardi, M. Leoni, S. Siboni, P. Scardi, *J. Appl. Crystallogr.* **2012**, 45, 1162-1172.

[68] A. Ulvestad, M. J. Welland, S. S. Collins, R. Harder, E. Maxey, J. Wingert, A. Singer, S. Hy, P. Mulvaney, P. Zapol, O. G. Shpyrko, *Nat. Commun.* **2015**, 6, 10092.

[69] J. Wu, L. Qi, H. You, A. Gross, J. Li, H. Yang, *J. Am. Chem. Soc.* **2012**, 134, 11880-11883.

[70] M. Li, Z. Zhao, T. Cheng, A. Fortunelli, C.-Y. Chen, R. Yu, Q. Zhang, L. Gu, B. Merinov, Z. Lin, E. Zhu, T. Yu, Q. Jia, J. Guo, L. Zhang, W. A. Goddard, Y. Huang, X. Duan, *Science* **2016**, 354, 1414-1419.

[71] R. Wang, C. Xu, X. Bi, Y. Ding, *Energy Environ. Sci.* **2012**, 5, 5281-5286.

[72] M. Escudero-Escribano, P. Malacrida, M. H. Hansen, U. G. Vej-Hansen, A. Velázquez-

Palenzuela, V. Tripkovic, J. Schiøtz, J. Rossmeisl, I. E. L. Stephens, I. Chorkendorff, *Science* **2016**, 352, 73-76.

[73] D. Wang, H. L. Xin, R. Hovden, H. Wang, Y. Yu, D. A. Muller, F. J. DiSalvo, H. D. Abruña, *Nat. Mater.* **2012**, 12, 81-87.

[74] L. Gan, R. Yu, J. Luo, Z. Cheng, J. Zhu, *J. Phys. Chem. Lett.* **2012**, 3, 934-938.

[75] X. Wang, S.-I. Choi, L. T. Roling, M. Luo, C. Ma, L. Zhang, M. Chi, J. Liu, Z. Xie, J. A. Herron, M. Mavrikakis, Y. Xia, *Nat. Commun.* **2015**, 6, 7594.

[76] T. Bian, H. Zhang, Y. Jiang, C. Jin, J. Wu, H. Yang, D. Yang, *Nano Lett.* **2015**, 15, 7808-7815.

[77] Z. Fan, Y. Zhu, X. Huang, Y. Han, Q. Wang, Q. Liu, Y. Huang, L. Gan Chee, H. Zhang, *Angew. Chem. Int. Ed.* **2015**, 54, 5672-5676.

[78] Z. Fan, Y. Chen, Y. Zhu, J. Wang, B. Li, Y. Zong, Y. Han, H. Zhang, *Chem. Sci.* **2017**, 8, 795-799.

[79] Z. Fan, Z. Luo, X. Huang, B. Li, Y. Chen, J. Wang, Y. Hu, H. Zhang, *J. Am. Chem. Soc.* **2016**, 138, 1414-1419.

[80] H. Topsøe, B. S. Clausen, R. Candia, C. Wivel, S. Mørup, *J. Catal.* **1981**, 68, 433-452.

[81] H. Topsøe, B. S. Clausen, *Catal. Rev.* **1984**, 26, 395-420.

[82] S. Eijsbouts, S. W. Mayo, K. Fujita, *Appl. Catal. A* **2007**, 322, 58-66.

[83] Q. Lu, Y. Yu, Q. Ma, B. Chen, H. Zhang, *Adv. Mater.* **2016**, 28, 1917-1933.

[84] D. Voiry, J. Yang, M. Chhowalla, *Adv. Mater.* **2016**, 28, 6197-6206.

[85] R. R. Chianelli, A. F. Ruppert, S. K. Behal, B. H. Kear, A. Wold, R. Kershaw, *J. Catal.* **1985**, 92, 56-63.

[86] D. Merki, X. Hu, *Energy Environ. Sci.* **2011**, 4, 3878-3888.

[87] A. B. Laursen, S. Kegnaes, S. Dahl, I. Chorkendorff, *Energy Environ. Sci.* **2012**, 5, 5577-5591.

[88] J. D. Benck, T. R. Hellstern, J. Kibsgaard, P. Chakthranont, T. F. Jaramillo, *ACS Catal.*

2014, 4, 3957-3971.

[89] Y. Yan, B. Xia, Z. Xu, X. Wang, *ACS Catal.* **2014**, 4, 1693-1705.

[90] X. Hong, K. Chan, C. Tsai, J. K. Nørskov, *ACS Catal.* **2016**, 6, 4428-4437.

[91] M. Asadi, B. Kumar, A. Behranginia, B. A. Rosen, A. Baskin, N. Repnin, D. Pisasale, P. Phillips, W. Zhu, R. Haasch, R. F. Klie, P. Král, J. Abiade, A. Salehi-Khojin, *Nat. Commun*. **2014**, 5, 4470.

[92] L. Zhang, X. Ji, X. Ren, Y. Ma, X. Shi, Z. Tian, M. Asiri Abdullah, L. Chen, B. Tang, X. Sun, *Adv. Mater.* **2018**, 30, 1800191.

[93] H. J. Conley, B. Wang, J. I. Ziegler, R. F. Haglund, S. T. Pantelides, K. I. Bolotin, *Nano Lett.* **2013**, 13, 3626-3630.

[94] K. He, C. Poole, K. F. Mak, J. Shan, *Nano Lett.* **2013**, 13, 2931-2936.

[95] Y. Y. Hui, X. Liu, W. Jie, N. Y. Chan, J. Hao, Y.-T. Hsu, L.-J. Li, W. Guo, S. P. Lau, *ACS Nano* **2013**, 7, 7126-7131.

[96] C. Rice, R. J. Young, R. Zan, U. Bangert, D. Wolverson, T. Georgiou, R. Jalil, K. S. Novoselov, *Phys. Rev. B* **2013**, 87, 081307.

[97] C. R. Zhu, G. Wang, B. L. Liu, X. Marie, X. F. Qiao, X. Zhang, X. X. Wu, H. Fan, P. H. Tan, T. Amand, B. Urbaszek, *Phys. Rev. B* **2013**, 88, 121301.

[98] C. Lee, X. Wei, J. W. Kysar, J. Hone, *Science* **2008**, 321, 385-388.

[99] S. Bertolazzi, J. Brivio, A. Kis, *ACS Nano* **2011**, 5, 9703-9709.

[100] A. Castellanos-Gomez, M. Poot, G. A. Steele, H. S. J. van der Zant, N. Agraït, G. Rubio-Bollinger, *Adv. Mater.* **2012**, 24, 772-775.

[101] F. Guinea, M. I. Katsnelson, A. K. Geim, *Nat. Phys.* **2010**, 6, 30-33.

[102] E. Scalise, M. Houssa, G. Pourtois, V. Afanas'ev, A. Stesmans, *Nano Res.* **2012**, 5, 43-48.

[103] W. S. Yun, S. W. Han, S. C. Hong, I. G. Kim, J. D. Lee, *Phys. Rev. B* **2012**, 85, 033305.

[104] H. Shi, H. Pan, Y.-W. Zhang, B. I. Yakobson, *Phys. Rev. B* **2013**, 87, 155304.

[105] T. M. G. Mohiuddin, A. Lombardo, R. R. Nair, A. Bonetti, G. Savini, R. Jalil, N. Bonini, D. M. Basko, C. Galiotis, N. Marzari, K. S. Novoselov, A. K. Geim, A. C. Ferrari, *Phys. Rev. B* **2009**, 79, 205433.

[106] M. Huang, H. Yan, C. Chen, D. Song, T. F. Heinz, J. Hone, *Proc. Natl. Acad. Sci. USA* **2009**, 106, 7304-7308.

[107] O. Frank, G. Tsoukleri, J. Parthenios, K. Papagelis, I. Riaz, R. Jalil, K. S. Novoselov, C. Galiotis, *ACS Nano* **2010**, 4, 3131-3138.

[108] F. Ding, H. Ji, Y. Chen, A. Herklotz, K. Dörr, Y. Mei, A. Rastelli, O. G. Schmidt, *Nano Lett.* **2010**, 10, 3453-3458.

[109] D. Lloyd, X. Liu, N. Boddeti, L. Cantley, R. Long, M. L. Dunn, J. S. Bunch, *Nano Lett.* **2017**, 17, 5329-5334.

[110] J.-K. Lee, S. Yamazaki, H. Yun, J. Park, G. P. Kennedy, G.-T. Kim, O. Pietzsch, R. Wiesendanger, S. Lee, S. Hong, U. Dettlaff-Weglikowska, S. Roth, *Nano Lett.* **2013**, 13, 3494-3500.

[111] A. Castellanos-Gomez, R. Roldán, E. Cappelluti, M. Buscema, F. Guinea, H. S. J. van der Zant, G. A. Steele, *Nano Lett.* **2013**, 13, 5361-5366.

[112] S. T. Gill, J. H. Hinnefeld, S. Zhu, W. J. Swanson, T. Li, N. Mason, *ACS Nano* **2015**, 9, 5799-5806.

[113] A. Reserbat-Plantey, D. Kalita, Z. Han, L. Ferlazzo, S. Autier-Laurent, K. Komatsu, C. Li, R. Weil, A. Ralko, L. Marty, S. Guéron, N. Bendiab, H. Bouchiat, V. Bouchiat, *Nano Lett.* **2014**, 14, 5044-5051.

[114] A. P. Nayak, T. Pandey, D. Voiry, J. Liu, S. T. Moran, A. Sharma, C. Tan, C.-H. Chen, L.-J. Li, M. Chhowalla, J.-F. Lin, A. K. Singh, D. Akinwande, *Nano Lett.* **2014**, 15, 346-353.

[115] G. Tsoukleri, J. Parthenios, K. Papagelis, R. Jalil, A. C. Ferrari, A. K. Geim, K. S. Novoselov, C. Galiotis, *Small* **2009**, 5, 2397-2402.

[116] D. Lloyd, X. Liu, J. W. Christopher, L. Cantley, A. Wadehra, B. L. Kim, B. B. Goldberg, A. K. Swan, J. S. Bunch, *Nano Lett.* **2016**, 16, 5836-5841.

[117] J. Zabel, R. R. Nair, A. Ott, T. Georgiou, A. K. Geim, K. S. Novoselov, C. Casiraghi, *Nano Lett.* **2011**, 12, 617-621.

[118] H. Tomori, A. Kanda, H. Goto, Y. Ootuka, K. Tsukagoshi, S. Moriyama, E. Watanabe, D. Tsuya, *Appl. Phys. Express* **2011**, 4, 075102.

[119] T. Ling, D. Y. Yan, H. Wang, Y. Jiao, Z. Hu, Y. Zheng, L. Zheng, J. Mao, H. Liu, X. W. Du, M. Jaroniec, S. Z. Qiao, *Nat. Commun.* **2017**, 8, 1509.

[120] D. Voiry, R. Fullon, J. Yang, C. de Carvalho Castro e Silva, R. Kappera, I. Bozkurt, D. Kaplan, M. J. Lagos, P. E. Batson, G. Gupta, A. D. Mohite, L. Dong, D. Er, V. B. Shenoy, T. Asefa, M. Chhowalla, *Nat. Mater.* **2016**, 15, 1003-1009.

[121] J. Wang, M. Yan, K. Zhao, X. Liao, P. Wang, X. Pan, W. Yang, L. Mai, *Adv. Mater.* **2017**, 29, 1604464-n/a.

[122] W. Wei, Y. Dai, B. Huang, *Phys. Chem. Chem. Phys.* **2017**, 19, 663-672.

[123] K. Liang, Y. Yan, L. Guo, K. Marcus, Z. Li, L. Zhou, Y. Li, R. Ye, N. Orlovskaya, Y. H. Sohn, Y. Yang, *ACS Energy Lett.* **2017**, 2, 1315-1320.

[124] M. A. Lukowski, A. S. Daniel, F. Meng, A. Forticaux, L. Li, S. Jin, *J. Am. Chem. Soc.* **2013**, 135, 10274-10277.

[125] D. Voiry, H. Yamaguchi, J. Li, R. Silva, D. C. B. Alves, T. Fujita, M. Chen, T. Asefa, V. B. Shenoy, G. Eda, M. Chhowalla, *Nat. Mater.* **2013**, 12, 850-855.

[126] D. Voiry, M. Salehi, R. Silva, T. Fujita, M. Chen, T. Asefa, V. B. Shenoy, G. Eda, M. Chhowalla, *Nano Lett.* **2013**, 13, 6222-6227.

[127] Y. Gong, J. Lin, X. Wang, G. Shi, S. Lei, Z. Lin, X. Zou, G. Ye, R. Vajtai, B. I. Yakobson, H. Terrones, M. Terrones, Beng K. Tay, J. Lou, S. T. Pantelides, Z. Liu, W. Zhou, P. M. Ajayan, *Nat. Mater.* **2014**, 13, 1135-1142.

[128] C. L. Green, A. Kucernak, *J. Phys. Chem. B* **2002**, 106, 1036-1047.

[129] A. Azcatl, X. Qin, A. Prakash, C. Zhang, L. Cheng, Q. Wang, N. Lu, M. J. Kim, J. Kim, K. Cho, R. Addou, C. L. Hinkle, J. Appenzeller, R. M. Wallace, *Nano Lett.* **2016**, 16, 5437-5443.

[130] J. H. Lee, W. S. Jang, S. W. Han, H. K. Baik, *Langmuir* **2014**, 30, 9866-9873.

[131] Y. Tan, P. Liu, L. Chen, W. Cong, Y. Ito, J. Han, X. Guo, Z. Tang, T. Fujita, A. Hirata, M. W. Chen, *Adv. Mater.* **2014**, 26, 8023-8028.

[132] D. Y. Hwang, K. H. Choi, J. E. Park, D. H. Suh, *Phys. Chem. Chem. Phys.* **2017**, 19, 18356-18365.

[133] D. Y. Hwang, K. H. Choi, J. E. Park, D. H. Suh, *Nanoscale* **2017**, 9, 503-508.

[134] H. Li, M. Du, M. J. Mleczko, A. L. Koh, Y. Nishi, E. Pop, A. J. Bard, X. Zheng, *J. Am. Chem. Soc.* **2016**, 138, 5123-5129.

[135] D. Kong, H. Wang, J. J. Cha, M. Pasta, K. J. Koski, J. Yao, Y. Cui, *Nano Lett.* **2013**, 13, 1341-1347.

[136] Y. Jung, J. Shen, Y. Liu, J. M. Woods, Y. Sun, J. J. Cha, *Nano Lett.* **2014**, 14, 6842-6849.

[137] S. Dhar, V. Kranthi Kumar, T. H. Choudhury, S. A. Shivashankar, S. Raghavan, *Phys. Chem. Chem. Phys.* **2016**, 18, 14918-14926.

[138] S. Jing, Y. Hyun Deog, L. Yanliang, L. Yifei, Y. Yan, C. G. Lars, *Mater.. Res. Express* **2016**, 3, 064001.

[139] Y. Liang, H. D. Yoo, Y. Li, J. Shuai, H. A. Calderon, F. C. Robles Hernandez, L. C. Grabow, Y. Yao, *Nano Lett.* **2015**, 15, 2194-2202.

[140] Y. Jung, Y. Zhou, J. J. Cha, *Inorg. Chem. Front.* **2016**, 3, 452-463.

[141] M. R. Gao, M. K. Y. Chan, Y. Sun, *Nat. Commun.* **2015**, 6, 7493.

[142] H. Wang, Z. Lu, S. Xu, D. Kong, J. J. Cha, G. Zheng, P.-C. Hsu, K. Yan, D. Bradshaw, F. B. Prinz, Y. Cui, *Proc. Natl. Acad. Sci. USA* **2013**, 110, 19701-19706.

[143] H. Jeen, W. S. Choi, M. D. Biegalski, C. M. Folkman, I. C. Tung, D. D. Fong, J. W. Freeland, D. Shin, H. Ohta, M. F. Chisholm, H. N. Lee, *Nat. Mater.* **2013**, 12, 1057.

[144] A. Kushima, S. Yip, B. Yildiz, *Phys. Rev. B* **2010**, 82, 115435.

[145] O. Diaz-Morales, S. Raaijman, R. Kortlever, P. J. Kooyman, T. Wezendonk, J. Gascon, W. T. Fu, M. T. M. Koper, *Nat. Commun.* **2016**, 7, 12363.

[146] J. R. Petrie, H. Jeen, S. C. Barron, T. L. Meyer, H. N. Lee, *J. Am. Chem. Soc.* **2016**, 138, 7252-7255.

[147] K. A. Stoerzinger, W. S. Choi, H. Jeen, H. N. Lee, Y. Shao-Horn, *J. Phys. Chem. Lett.* **2015**, 6, 487-492.

[148] A. Forticaux, L. Dang, H. Liang, S. Jin, *Nano Lett.* **2015**, 15, 3403-3409.

[149] F. Gunkel, L. Jin, D. N. Mueller, C. Hausner, D. S. Bick, C.-L. Jia, T. Schneller, I. Valov, R. Waser, R. Dittmann, *ACS Catal*. **2017**, 7, 7029-7037.

[150] Q. Wang, D. O'Hare, *Chem. Rev.* **2012**, 112, 4124-4155.

[151] Z. Jeremie, T. M. Caspary, *ChemElectroChem* **2017**, 4, 2764-2770.

[152] S. M. Pawar, B. S. Pawar, B. Hou, J. Kim, A. T. Aqueel Ahmed, H. S. Chavan, Y. Jo, S. Cho, A. I. Inamdar, J. L. Gunjakar, H. Kim, S. Cha, H. Im, *J. Mater. Chem. A* **2017**, 5, 12747-12751.

[153] L. Cai, C. J. McClellan, A. L. Koh, H. Li, E. Yalon, E. Pop, X. Zheng, *Nano Lett.* **2017**, 17, 3854-3861.

The recent theoretical and experimental progresses of applying strain to enhance heterogeneous electrocatalysts (from zero-dimensional nanoparticles to one-dimensional nanowires/nanotubes, and then to two-dimensional nanosheets) for both hydrogen evolution reaction (HER) and oxygen evolution reaction (OER) has been reviewed. This review shows that elastic strain enriches the toolbox for improving electrocatalysts particularly for HER and OER.

Keywords: water splitting, electrocatalyst, strain engineering, two-dimensional materials, DFT modeling

Bo You[†], Michael T Tang[†], Charlie Tsai, Frank Abild-Pedersen, Xiaolin Zheng, and Hong Li*

Title: Enhancing Electrocatalytic Water Splitting by Strain Engineering

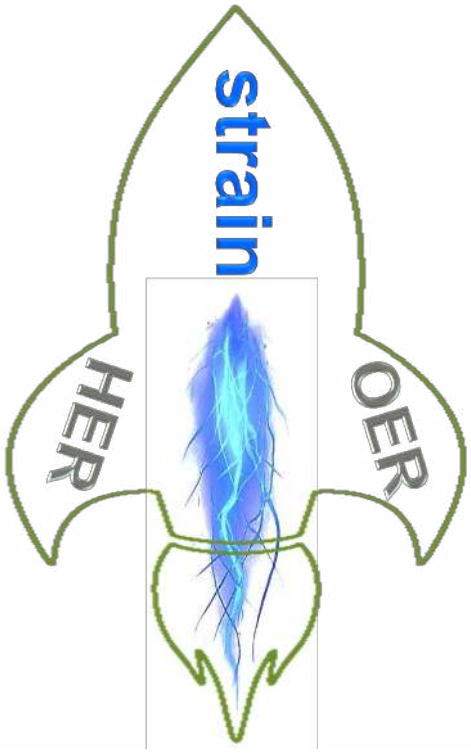

Click here to access/download
Supporting Information
Copyright forms.zip